THE GEOLOGICAL SOCIETY OF AMERICA®

Origin of Late Cretaceous, enclave-bearing granitoids in southern Tibet: Implications for magma recharge and crustal thickening

Ding-Jun Wen[1], Xiumian Hu[1,†], Jin-Hai Yu[1], Xiao-Lei Wang[1], Timothy Chapman[2], and Rui-Qiang Wang[3]
[1]*State Key Laboratory for Mineral Deposits Research, School of Earth Sciences and Engineering, Nanjing University, Nanjing 210023, China*
[2]*Earth Science, School of Environmental and Rural Science, University of New England, Armidale, NSW 2351, Australia*
[3]*School of Earth Science and Resources, China University of Geosciences, Beijing 100083, China*

ABSTRACT

Exposures of enclave-bearing granitoids can provide rare opportunities to directly evaluate the connection between compositional variability and the depth of origin of arc magmatic rocks. The ~1000 km long Gangdese batholith is a composite batholith with composition from mafic to felsic; SiO_2 ranges from 51 wt% to 70 wt%. New zircon U–Pb dating of the Nyemo plutons, Renbu plutons, and Xigaze plutons in the Gangdese batholith is consistent with their emplacement and crystallization in the Late Cretaceous (ca. 90–85 Ma). Mafic magmatic enclaves (MMEs) in the plutons are characterized by low SiO_2 (50.9–56.0 wt%) and Nb/U, Ce/Pb, and Nb/La ratios coupled with enrichment in light rare earth elements and large ion lithophile elements and depletion in high field strength elements. These geochemical features, combined with depleted whole-rock $\varepsilon_{Nd}(t)$ (+4.2 to +4.7) and zircon $\varepsilon_{Hf}(t)$ (+9.0 to +13.8), suggest that they were derived by partial melting of a depleted mantle source associated with subduction-related fluids. The granitoids with high SiO_2 (55.6–66.9 wt%) display adakitic geochemical characteristics, such as low Y and Yb contents, and high Sr/Y and La/Yb ratios. Their positive whole-rock $\varepsilon_{Nd}(t)$ (+4.0 to +5.5) and zircon $\varepsilon_{Hf}(t)$ (+6.9 to +14.3) values, as well as enrichment of incompatible elements, indicate that the granitoids were derived from partial melting of the juvenile lower crust. Geochemical modeling suggests that the compositional diversities of MMEs and adakitic granitoids were inherited from heterogeneous sources. This genetic relationship indicates that the underplated basaltic magmas could have supplied sufficient heat to trigger the melting of the thickened crust and thus formation of the enclave-bearing granitoid. In this regard, the origin of arc rocks can mirror the evolution of crustal thickness. Our results reveal that the crust was thickened to ~50 km during the Late Cretaceous (90–85 Ma) and provide a magmatic record of crustal thickening prior to the Cenozoic Indo-Asia collision.

INTRODUCTION

Continental arcs, like those represented around the modern Circum-Pacific (Hildreth and Moorbath, 1988; Farner and Lee, 2017), are characterized by alternating periods of magmatic flare-ups and lulls (Ardill et al., 2018). Arc-related mafic to felsic suites are produced in response to changes in tectonism during the subduction of oceanic lithosphere. It is widely acknowledged that mafic magmatism plays a critical role in the generation of voluminous calc-alkalic batholiths in convergent-margin settings. Mafic melts are the precursor magmas for crystal fractionation (Bateman and Chappell, 1979; Lee and Bachmann, 2014) and the end-member components of magma recharge and mixing (e.g., Allègre and Othman, 1980; Castro et al., 1991), and they act as heat sources for partial melting of the lower crust (e.g., Hildreth, 1981; Bergantz, 1989). Although common arc magmas are compositionally similar to the average bulk continental crust, which is enriched in large ion lithophile elements (LILEs) but depleted in high field strength elements (HFSEs) (e.g., Rudnick, 1995; Rudnick and Gao, 2003), there remains considerable controversy about the mechanisms responsible for generating arc magmatism. Understanding arc magmatism is crucial to evaluating models of the generation and evolution of continental crust.

Most mafic intrusive rocks are thought to originate from the partial melting of peridotite in the mantle wedge, which is associated with the fluxing of slab-derived fluids and/or possibly the pressure release of warmer mantle material from greater depths (Davies and Stevenson, 1992; Sisson and Bronto, 1998; Tamura et al., 2002). The origin of coexistent felsic suites has been attributed to interplays between fractional crystallization, partial melting, assimilation, and/or mixing (Hildreth and Moorbath, 1988; Ratajeski et al., 2001; Chapman et al., 2016; Farner et al., 2018) of magmas derived from basaltic rocks (Defant and Drummond, 1990; Yogodzinski et al., 1995; Stern and Kilian, 1996), metasedimentary rocks, or other basement rocks (Ducea et al., 2015). An alternative model suggests that silicic magmas in long-lived magma chambers are commonly stored as crystal mush within the cold mid–upper crust (Szymanowski et al., 2017; Tavazzani et al., 2020; Du et al., 2022). In this interpretation, the chemical diversity of magmatic rocks is mainly controlled by the differentiation of mantle-derived mafic melts along the liquid line of descent as crystal cumulates are left behind at various crustal depths (Moyen et al., 2021). Recently, a number of studies have revealed the connection between composition of the arc rock and crustal thickness and suggest that primary magma composition in the arc can be altered as a function of crustal thickness (Alasino et al., 2022). For example, some scholars have proposed that crustal thickness controls the composition of primary magmas by modulating the degree of mantle melting (Plank and Langmuir, 1988; Turner and Langmuir, 2015), whereas for other magmas, a series of intracrustal differentiation processes regulated by the crustal thickness dilutes the source signal (e.g., Hildreth and Moorbath, 1988; Lee and Bachmann, 2014; Farner and Lee, 2017). Although many studies have examined spatiotemporal and chemical trends of the coexistent arc-related mafic to felsic

†Corresponding author: School of Earth Sciences and Engineering, Nanjing University, Nanjing 210023, China; huxm@ nju.edu.cn.

 https://doi.org/10.1130/B36530.1; 14 figures; 1 supplemental file.

suites (e.g., Bateman, 1992; Lackey et al., 2012; Klein et al., 2021), the detailed processes regarding how and where magmas interact and differentiate within the crust are not well understood (Annen et al., 2006; Bachmann et al., 2007). In this context, felsic intrusive rocks with abundant mafic magmatic enclaves (MMEs) provide an excellent opportunity to explore these questions. The enclave-bearing granitoids studied here from the Gangdese batholith add to other well-studied examples, such as in the Halfmoon Pluton, New Zealand (Turnbull et al., 2010), Aegean arc, Greece (Klaver et al., 2017), Adamello Massif, Italy (Blundy and Sparks, 1992; Pistone et al., 2017), northern Peninsular Ranges batholith and Sierra Nevada batholith, California (Barbarin, 2005; Farner et al., 2018), and Central Victoria, Australia (Clemens et al., 2017).

Here, we present new mineralogy, geochronology, and whole-rock geochemical data for the mafic to felsic Nyemo plutons, Renbu plutons, and Xigaze plutons in the Gangdese batholith in southern Tibet. Our results, combined with previously published data for the coeval intrusive rocks in the region, are used to explore the following fundamental questions regarding the Late Cretaceous granitoids and MMEs in the southern Lhasa subterrane: (1) what is the genetic link between the contemporary mafic and felsic arc magmatism?, (2) do these mafic to felsic rocks reflect the thickening of regional crust since the Late Cretaceous?, and (3) if so, how was the crust thickened and then uplifted?

GEOLOGICAL SETTING AND SAMPLING

The Himalayan-Tibetan plateau is a continent-continent collisional zone that was formed by the northward accretion of several roughly east–west-trending terranes. These terranes include (from north to south) the Songpan–Ganze terrane, Qiangtang terrane, Lhasa terrane, and the Tethyan Himalaya (Fig. 1A; Yin and Harrison, 2000). The Lhasa terrane is sandwiched between the Tethyan Himalaya to the south and the Qiangtang terrane to the north by the Indus–Yarlung Zangbo and the Bangong–Nujiang suture zones, respectively (Yin and Harrison, 2000; Zhu et al., 2013). According to the distribution of the ophiolites and the nature of the crystalline basement, the Lhasa terrane can be subdivided into the northern, central, and southern subterranes, which are bounded approximately by the Shiquan River–Nam Tso mélange zone and the Luobadui–Milashan Fault, respectively (Fig. 1B; Zhu et al., 2009). The northern Lhasa subterrane is mainly composed of Triassic–Cenozoic sedimentary rocks, Early Cretaceous intrusive rocks, and their volcanic counterparts (Zhu et al., 2011). In comparison, the central Lhasa subterrane was once a microcontinent with Archean–Proterozoic basement (Zhu et al., 2011) overlain by a Carboniferous–Permian metasedimentary sequence and Late Jurassic–Early Cretaceous volcanic-sedimentary rocks, with minor late Mesozoic intrusive rocks (Kapp et al., 2005; Leier et al., 2007; Zhu et al., 2011). The southern Lhasa subterrane comprises the Gangdese batholith and Early Jurassic–Cenozoic volcanic succession (Fig. 1B; Mo et al., 2008; Ji et al., 2009; Chapman and Kapp, 2017), with the latter consisting of the Early Jurassic Yeba Formation, the Sangri Group, and the Cenozoic Linzizong volcanic succession (Zhu et al., 2013). Geochronological studies reveal that arc magmatism in the Gangdese started in the Late Triassic and persisted until the Paleocene, with two magmatic flare-up events at ca. 190 Ma and ca. 90 Ma (Ji et al., 2009; Ma et al., 2013a; Zhu et al., 2011). The temporal and spatial distribution of the Gangdese arc magmatism is likely related to variations in the subduction angle of the Neo-Tethyan oceanic slab (Kapp et al., 2005;

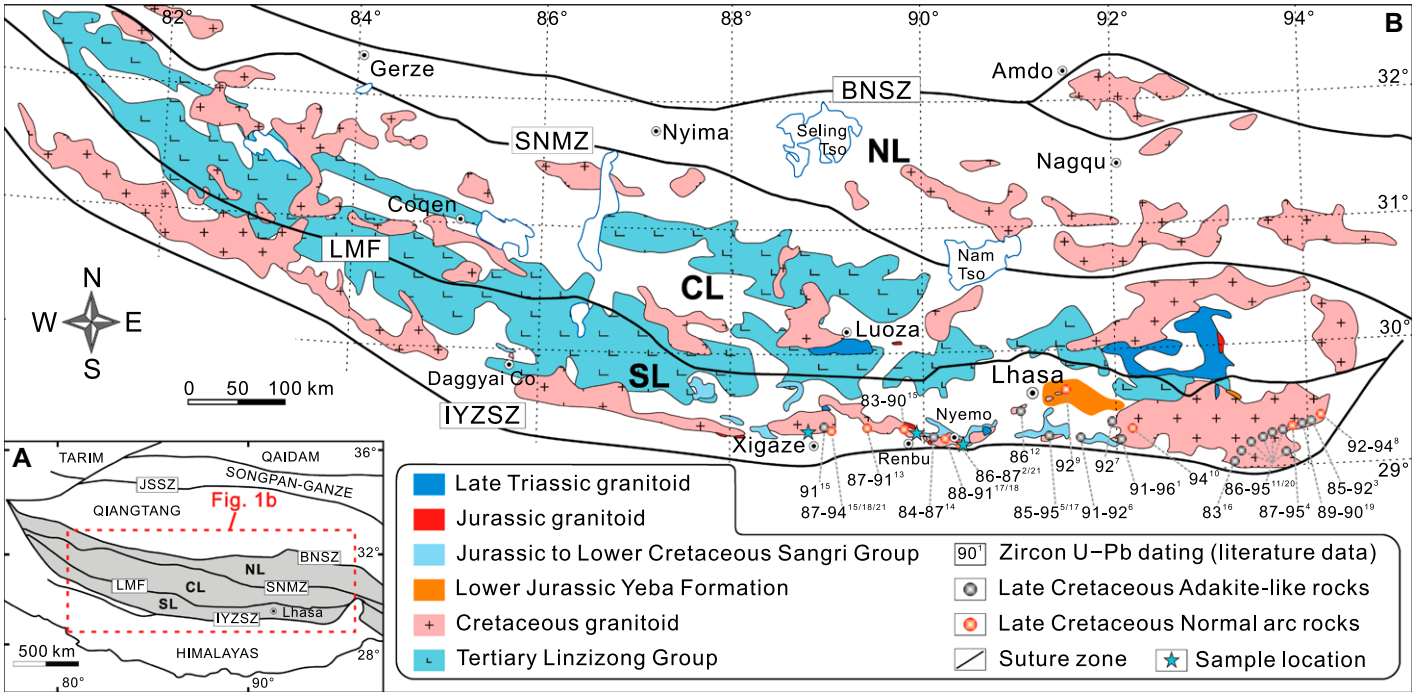

Figure 1. (A) Simplified tectonic map of the Tibetan Plateau shows the location of the Lhasa terrane. (B) Geological map of the Lhasa terrane shows major tectonic subdivisions and the temporal and spatial distribution of Late Cretaceous magmatism (modified from Zhu et al., 2013). Ages for Late Cretaceous igneous rocks in the Gangdese area (i.e., the southern Lhasa subterrane) are from Table S1 (see text footnote 1). Abbreviations are as follows: JSSZ—Jinshajiang suture zone, BNSZ—Bangong–Nujiang suture zone, SNMZ—Shiquan River–Nam Tso mélange zone, LMF—Luobadui–Milashan Fault, IYZSZ—Indus–Yarlung Zangbo suture zone, SL—southern Lhasa subterrane, CL—central Lhasa subterrane, and NL—northern Lhasa subterrane.

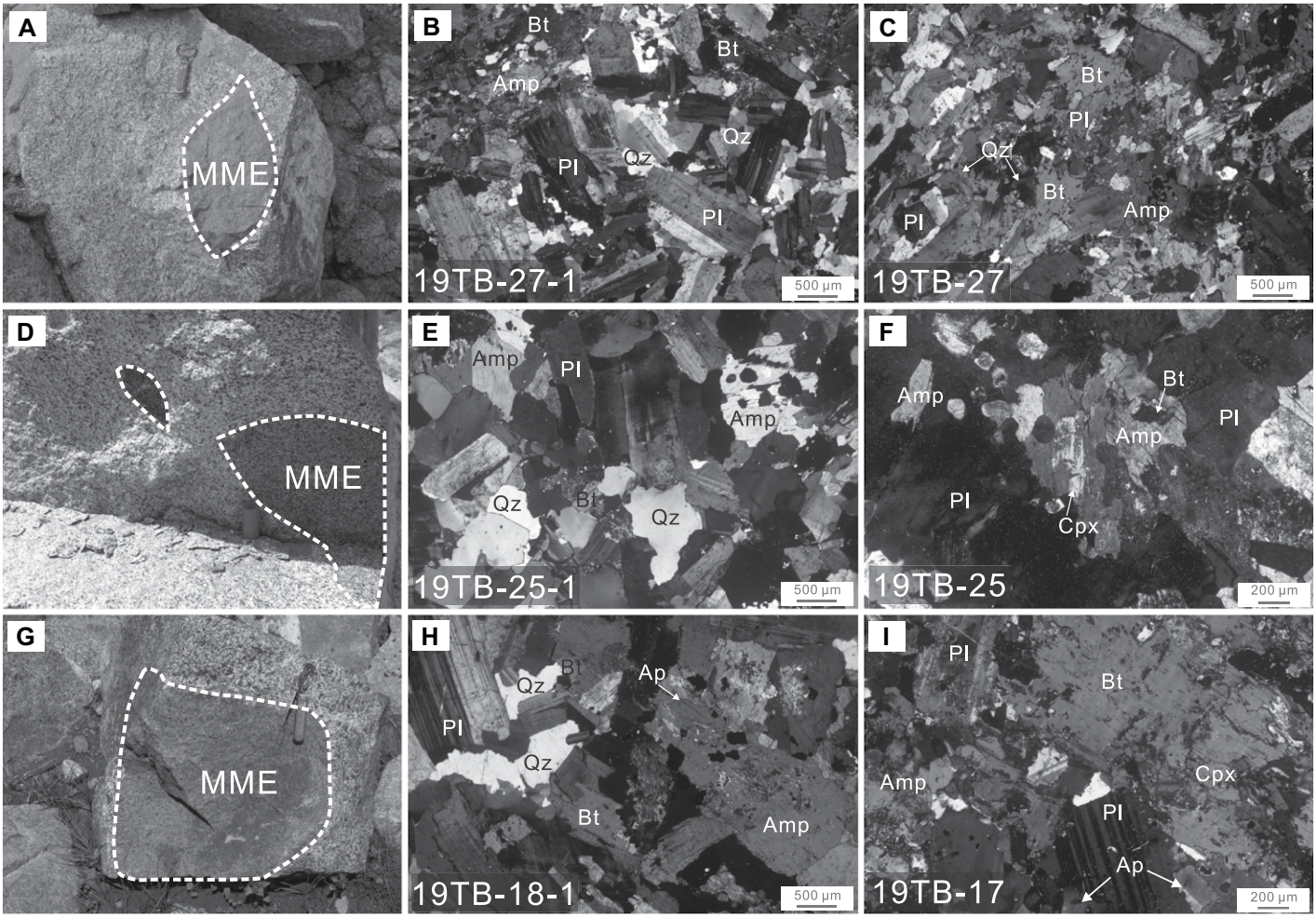

Figure 2. (A, D, and G) Photographs of field outcrops and (B, C, E, F, H, and I) representative photomicrographs (under cross-polarized light) of the Nyemo plutons, Renbu plutons, and Xigaze plutons from the Gangdese batholith are shown. Mineral abbreviations: Ap—apatite; Amp—amphibole; Bt—biotite; Pl—plagioclase; Qz—quartz; MME—mafic magmatic enclave.

Ma et al., 2013a). In this study, we focus on three subduction-related plutons (Fig. 1B; Nyemo plutons in the Nyemo area, Renbu plutons in the Renbu area, and Xigaze plutons in the Xigaze area) in the southern Lhasa subterrane.

The diorites and granodiorites are the dominant rocks (>90 vol%) of the Nyemo plutons, and there are minor enclaves (15–30 cm in diameter; Fig. 2A). The granodiorite is fine- to medium-grained (1–3 mm) and consists of hornblende (15%), biotite (5%), plagioclase (55%), K-feldspar (5%), and quartz (20%), with minor amounts of zircon, magnetite, and apatite (Fig. 2B). The equigranular and fine-grained (1–2 mm) MMEs (e.g., sample 19TB-27) consist of hornblende (20%), biotite (10%), plagioclase (55%), K-feldspar (5%), and quartz (10%), and accessory titanite, magnetite, and apatite (Fig. 2C).

The Renbu plutons are composed of quartz diorites and granodiorites with MMEs (~5 vol%) in different shapes (Fig. 2D). The felsic host is fine- to medium-grained (1–3 mm) and consists of hornblende (10%), biotite (5%), plagioclase (50%), K-feldspar (15%), and quartz (20%) with minor amounts of zircon, titanite, and apatite (Fig. 2E). The equigranular and fine-grained MMEs (e.g., sample 19TB-25) consist of hornblende (25%), biotite (10%), plagioclase (55%), K-feldspar (5%), and quartz (5%), along with accessory clinopyroxene, titanite, and apatite (Fig. 2F).

The Xigaze plutons are composed of dioritic host and ~20 vol% MMEs (Fig. 2G). The MMEs show sharp contacts against the host diorite. The diorite is medium- to coarse-grained (2–3 mm) and consists of hornblende (20%), biotite (10%), plagioclase (50%), K-feldspar (10%), and quartz (10%), with minor amounts of accessory zircon and apatite (Fig. 2H). The MMEs (e.g., sample 19TB-18) have variable shapes and sizes (up to ~30 cm; Fig. 2G) and consist of hornblende (30%), biotite (5%), plagioclase (65%), and accessory clinopyroxene, zircon, and apatite (Fig. 2I).

ANALYTICAL METHODS

Zircon U–Pb Dating and Hf Isotopes

Zircon grains were extracted by conventional heavy-liquid and magnetic separation techniques from crushed rocks. Cathodoluminescence (CL) images of the zircon grains analyzed were obtained using a JEOL JXA-8100 microprobe at the State Key Laboratory for Mineral Deposits Research, Nanjing University, Nanjing, China (MiDeR-NJU). Zircon U–Pb isotopic analyses were conducted by laser ablation–inductively coupled plasma–mass spectrometer (LA–ICP–MS) using a Thermo Scientific™ ICAP™ RQ quadrupole ICP–MS equipped with a Coher-

ent GeoLas Pro 193 nm laser ablation system at MiDeR-NJU. Analyses were performed with a laser beam diameter of 32 μm, a 5 Hz repetition rate, and an energy of 10–20 J/cm^2. The ablated material was transported in an He carrier gas through PVC tubing (inner diameter of 3 mm) and then combined with Ar in a 30 cm^3 mixing chamber before entering the ICP-MS for isotopic quantification. Each run included ~10–13 unknowns and two zircon reference material analyses (GEMOC GJ-1; $^{207}Pb/^{206}Pb$ age of 608.5 ± 1.5 Ma; Jackson et al., 2004) at the beginning and end of the run, respectively. The zircon standard "Mud Tank," with a reported age of 732 ± 5 Ma (Black and Gulson, 1978), was analyzed in every run after two GEMOC GJ-1 analyses as an independent monitor of the analytical accuracy. The raw U–Pb isotopic data were acquired using GLITTER software (version 4.4; http://www.glitter-gemoc.com/), and common Pb corrections were calculated following Andersen (2002). Concordia diagrams and weighted mean calculations were made using Isoplot/Ex_ver3 (Ludwig, 2003).

Zircon Hf isotope analyses were carried out in situ using a Coherent GeoLas Pro 193 nm LA system combined with a Thermo Scientific™ Neptune Plus™ MC–ICP–MS at the MiDeR-NJU. Analyses were carried out with a beam diameter of 44 μm. The detailed instrumental conditions and interference correction method utilized were those described by Wu et al. (2006). To evaluate the reliability and stability of the instrument, the standard "Mud Tank" was analyzed during the study and yielded a mean $^{176}Hf/^{177}Hf$ value of 0.282495 ± 10 (2SD, n = 52), which is consistent with the recommended values within error (Woodhead and Hergt, 2005).

The initial $^{176}Hf/^{177}Hf$ ratios were calculated using the ^{176}Lu decay constant of 1.867×10^{-11} yr^{-1} (Söderlund et al., 2004). The chondritic values of $^{176}Hf/^{177}Hf = 0.282772$ and $^{176}Lu/^{177}Hf = 0.0332$ reported by Blichert-Toft and Albarède (1997) were adopted to calculate the $\varepsilon_{Hf}(t)$ values. The depleted mantle Hf model age (T_{DM}) was calculated using the depleted mantle values with a present-day value of $^{176}Lu/^{177}Hf = 0.0384$ and $^{176}Hf/^{177}Hf = 0.28325$ (Griffin et al., 2000). The crustal model age (T_{DMC}) was calculated using a $^{176}Lu/^{177}Hf$ value of 0.015 for the average crust (Griffin et al., 2002).

Whole-Rock Major and Trace Element and Sr–Nd Isotope Analyses

Whole-rock major element concentrations were analyzed by a Thermo Scientific ARL 9900 X-ray fluorescence spectrometer (XRF) at the Centre of Modern Analysis, Nanjing University, with a precision of better than 5% for all elements. Trace element (including rare earth element [REE]) abundances were measured using an Agilent 7700e ICP-MS at the Wuhan Sample Solution Analytical Technology Co., Ltd., Wuhan, China. For a detailed sample-digesting procedure and analytical precision and accuracy for the trace elements, see Zong et al. (2017).

For whole-rock Sr–Nd isotope analyses, ~50 mg of powder was digested in a Teflon beaker with a HF + HNO_3 mixture. Rb–Sr and Sm–Nd were separated using AG® 50W-X8 resin and various eluents. Rare earth elements were first separated from Rb–Sr by conventional cation exchange chromatography using HCl as an eluent. Rb and Sr were then separated and purified using a mixed eluent of pyridinium and DCTA complex. Sm and Nd were separated and purified using HIBA as an eluent through a small volume of cation exchange resin (0.6 mL). The isotopic compositions of purified Sr and Nd solutions were determined at the MiDeR-NJU. Sr isotopic compositions were measured using a Finnigan TRITON thermal ionization mass spectrometer. Nd isotopic compositions were measured using a Thermo Scientific™ Neptune Plus™ MC–ICP–MS. For details of the chemical separation and isotopic measurement procedures followed, see Pu et al. (2005). $^{87}Sr/^{86}Sr$ and $^{143}Nd/^{144}Nd$ ratios are reported as measured, after normalization to $^{86}Sr/^{88}Sr = 0.1194$ and $^{146}Nd/^{144}Nd = 0.7219$, respectively, to correct for instrumental fractionation. Repeat measurements of the Japan JNdi-1 Nd standard yielded $^{143}Nd/^{144}Nd = 0.512108 \pm 0.000006$, and repeat measurements of the NIST SRM 987 Sr standard yielded $^{87}Sr/^{86}Sr = 0.710230 \pm 0.000005$.

Mineral Chemistry

Mineral compositions were analyzed at the electron microprobe laboratory of the MiDeR-NJU using a JEOL JXA-8230 electron microprobe. The operating conditions were set to an acceleration voltage of 15 kV, a beam current of 20 nA, and a beam diameter of 5 μm for analysis of amphiboles.

ANALYTICAL RESULTS

Zircon U–Pb Geochronology

Zircon crystals from the Nyemo plutons, Renbu plutons, and Xigaze plutons are euhedral to subhedral and show clear oscillatory zoning in cathodoluminescence (CL) images and high Th/U values (typically >0.35; Fig. 3; Supplemental Material Table S2[1]). These features are consistent with a magmatic origin (Hoskin and Schaltegger, 2003). Therefore, the U–Pb zircon ages were interpreted to represent the crystallization age of the magmatic rocks.

The analyses of zircon grains from the felsic rock (diorite and granodiorite) samples (16TB-24, 16TB-27, and 19TB-27–1) and the MME sample (19TB-27) from the Nyemo plutons are concordant and yielded weighted mean $^{206}Pb/^{238}U$ ages of 84.8 ± 0.9 Ma (n = 22; MSWD = 0.5), 86.7 ± 0.6 Ma (n = 21; MSWD = 1.1), 88.9 ± 0.5 Ma (n = 21; MSWD = 0.8), and 89.7 ± 0.5 Ma (n = 24; MSWD = 0.3), respectively (Figs. 3A–3D). Two data points from the felsic rock (19TB-27–1) are discordant, with $^{206}Pb/^{238}U$ ages of 85 Ma and 95 Ma. One older analysis with $^{206}Pb/^{238}U$ age of 214 Ma shows characteristics of a magmatic zircon in CL images and was likely inherited from an older crustal component. One data point from an MME (19TB-27–1) is discordant, with $^{206}Pb/^{238}U$ ages of 94 Ma. A total of 25 sites from granodiorite sample 19TB-25-1 and 25 sites from MME sample 19TB-25 were analyzed and yielded weighted mean $^{206}Pb/^{238}U$ ages of 89.0 ± 0.5 Ma (n = 24; MSWD = 1.1) and 87.4 ± 0.4 Ma (n = 25; MSWD = 0.7), respectively (Figs. 3E and 3F). Two diorite samples from the Xigaze plutons (19TB-18–1 and TB-16–1) were analyzed and yield weighted mean $^{206}Pb/^{238}U$ ages of 89.9 ± 0.7 Ma (n = 22; MSWD = 0.5) and 85.1 ± 1.1 Ma (n = 18; MSWD = 0.8), respectively (Figs. 3G and 3H). Three analyses of sample 19TB-18-1 recorded older $^{206}Pb/^{238}U$ ages of 196–200 Ma and defined a weighted mean $^{206}Pb/^{238}U$ age of 197.3 ± 3.7 Ma (MSWD = 0.3), and these zircon grains were interpreted as a xenocryst. Five data points from the sample TB-16-1 were discordant, with $^{206}Pb/^{238}U$ ages of 80 Ma and 88 Ma.

Zircon Hf Isotopic Compositions

Zircon grains from seven representative samples were chosen for Hf isotope analysis. The zircon Hf isotopic compositions are listed in Table S3 (see footnote 1). Three fel-

[1]Supplemental Material. Table S1: Results of synthesized age data. Table S2: Zircon U–Pb dating. Table S3: Zircon Hf isotopic compositions. Table S4: Whole-rock chemical compositions. Table S5: Whole-rock Sr–Nd isotopic compositions. Table S6: Mineral EMPA analysis. Table S7: Non-modal batch melting modeling. Please visit https://doi.org/10.1130/GSAB.S.21397245 to access the supplemental material, and contact editing@geosociety.org with any questions.

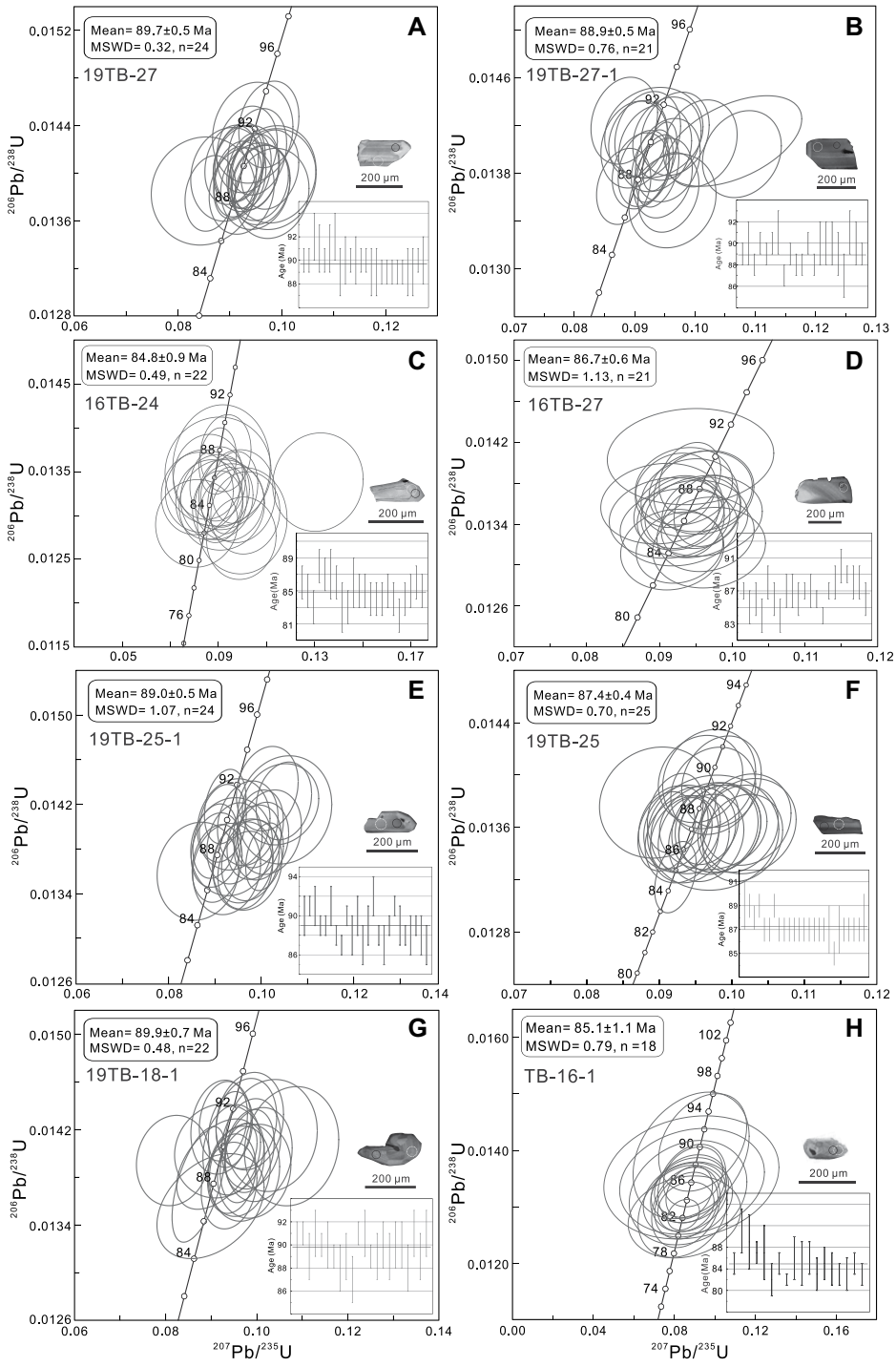

Figure 3. Laser ablation–inductively coupled plasma–mass spectrometry zircon U–Pb concordia diagrams are shown for the Nyemo plutons, Renbu plutons, and Xigaze plutons from the Gangdese batholith along with representative zircon cathodoluminescence images. Black and white circles denote the spot locations of U–Pb age and in situ Hf isotope analyses, respectively.

sic rock (diorite and granodiorite) samples of the Nyemo plutons (16TB-24, 16TB-27, and 19TB-27-1) were analyzed, and these samples have similar Hf isotopic compositions. Twenty Hf isotopic analyses on 20 zircon grains from sample 16TB-24 revealed $\varepsilon_{Hf}(t)$ values of +6.9 to +12.7 and two-stage Hf model ages, T_{DM2} (Hf), of 0.71–0.34 Ga. Nineteen spot analyses on 19 zircon grains from sample 16TB-27 yielded $\varepsilon_{Hf}(t)$ values of +9.0 to +12.0 and T_{DM2} (Hf) of 0.58–0.39 Ga. Fourteen spot analyses on 14 zircon grains from sample 19TB-27-1 gave $\varepsilon_{Hf}(t)$ values of +11.8 to +13.0 and T_{DM2} (Hf) of 0.40–0.33 Ga. In addition, the MMEs from sample 19TB-27 show relatively homogeneous $\varepsilon_{Hf}(t)$ values of +11.9 to +13.3 (n = 12), with T_{DM2} (Hf) of 0.39–0.30 Ga.

Twelve spot analyses on zircon grains from granodiorite sample 19TB-25-1 from the Renbu plutons revealed $\varepsilon_{Hf}(t)$ values of +12.5 to +13.6 and T_{DM2} (Hf) of 0.35–0.28 Ga. Sixteen spot analyses on zircon grains from the MMEs (19TB-25) of the Renbu plutons gave $\varepsilon_{Hf}(t)$ values of +11.9 to +13.8 and T_{DM2} (Hf) of 0.39–0.27 Ga. Thirteen spot analyses on zircon grains from diorite sample 19TB-18-1 from the Xigaze plutons revealed $\varepsilon_{Hf}(t)$ values of +11.0 to +12.8 and T_{DM2} (Hf) of 0.45–0.33 Ga.

Whole-Rock Major and Trace Elements

Whole-rock major- and trace-element data for the Nyemo plutons, Renbu plutons, and Xigaze plutons are provided in Table S4 (see footnote 1). Most samples are subalkaline in the SiO_2 versus $Na_2O + K_2O$ total alkali-silica (TAS) diagram (Fig. 4A). The granitoids in the Nyemo plutons, Renbu plutons, and Xigaze plutons have variable SiO_2 (55.57–66.89 wt%), K_2O (1.41–4.69 wt%), and MgO (1.63–4.44 wt%). They plot in the high-K calc-alkaline field on the SiO_2 versus K_2O diagram and are metaluminous with A/CNK [molar $Al_2O_3/(CaO + Na_2O + K_2O)$] ratios of 0.80–0.95 (Figs. 4B–4D). The MMEs in the Nyemo plutons, Renbu plutons, and Xigaze plutons have low SiO_2 (50.91–56.00 wt%), K_2O (1.02–2.92 wt%), and high MgO (3.90–6.07 wt%). They fall in the domains of high-K calc-alkaline to calc-alkaline on the SiO_2 versus K_2O diagram (Fig. 4B) and are metaluminous with A/CNK ratios of 0.73–0.80 (Fig. 4D). In the Harker diagrams (Fig. 5), all of these samples form clearly continuous major element variation arrays with the coeval gabbros. Most of the felsic rocks have lower heavy rare earth elements (HREE; Yb = 0.94–2.95 ppm) and Y concentrations (10.7–32.1 ppm), as well as high Sr (329–801 ppm) relative to those of MMEs. Therefore, these felsic rocks exhibit an adakite-like characteristic according to the definition of Defant and Drummond (1990), which is supported by the distribution of compositions on La/Yb_N versus Yb_N and Sr/Y versus Y discrimination diagrams (Figs. 6A and 6B). In addition, these felsic rocks mostly have relatively low Cr (2.67–71.0 ppm) and Ni (6.77–39.3 ppm) contents (Figs. 6C and 6D), which are also similar

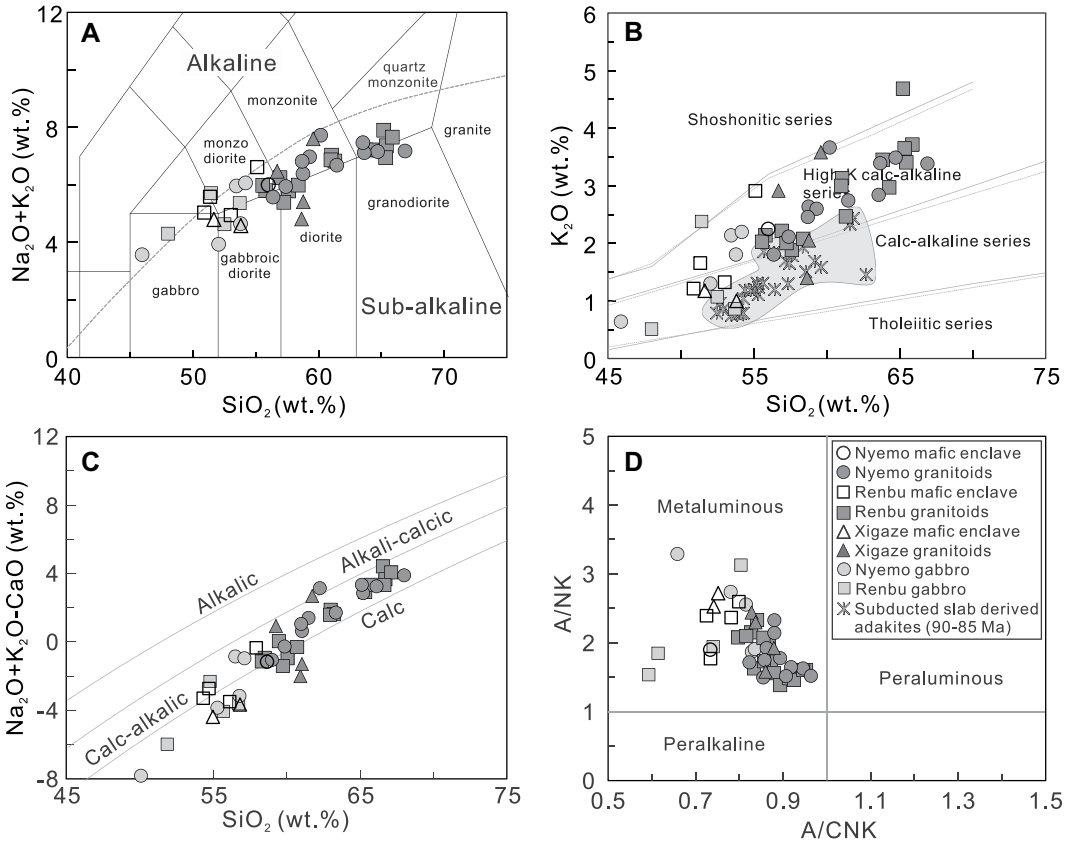

Figure 4. Chemical classification diagrams for the Nyemo plutons, Renbu plutons, and Xigaze plutons are shown. (A) Silica versus total alkalis diagram (Middlemost, 1994). (B) SiO_2 versus K_2O plot (Peccerillo and Taylor, 1976). (C) SiO_2 versus $Na_2O + K_2O$–CaO diagram (Frost et al., 2001). (D) A/CNK (molecular Al_2O_3 /[CaO + Na_2O + K_2O]) versus A/NK (molecular Al_2O_3 / [Na_2O + K_2O]) plot (Shand, 1943). Data for slab-derived, sodium-rich adakites (90–85 Ma) of the Gangdese batholith are from Zhang et al. (2010) and Yin et al. (2020).

to those of adakites derived from the thickened lower crust (Wang et al., 2006).

In the chondrite-normalized rare earth element (REE) diagram (Figs. 7A–7C), both the felsic rocks and MMEs are characterized by a flat HREE pattern ($[Dy/Yb]_N = 0.93–1.42$ for felsic rocks and $[Dy/Yb]_N = 0.96–1.38$ for MMEs) and slightly negative Eu anomalies (Eu/Eu* = 0.56–1.02 for felsic rocks and Eu/Eu* = 0.59–1.07 for MMEs). The felsic rock samples are enriched in LILEs (Rb, Th, and K) but depleted in HFSEs such as Nb, Ta, and Ti (Figs. 7D–7F). Compared to the felsic rocks, the MMEs exhibit less enrichment of incompatible elements (e.g., Rb, Th, U, Nb, Ta, Zr, and Hf) and light rare earth elements (LREEs; Fig. 7).

Whole-Rock Sr–Nd Isotopic Compositions

Whole-rock Sr–Nd isotopic compositions of representative samples from the Nyemo plutons, Renbu plutons, and Xigaze plutons are listed in Table S5 (see footnote 1). For comparison, the initial isotopic ratios of all samples are calculated at 90 Ma. The felsic rocks have depleted Sr–Nd isotopic compositions, with initial $^{87}Sr/^{86}Sr$ ratios of 0.7038–0.7044 and $\varepsilon_{Nd}(t)$ values of +4.0 to +5.5, which correspond to a young two-stage Nd model age (T_{DM2}[Nd]) of 0.62–0.45 Ga. The MMEs have similar Sr–Nd isotopic compositions, with $^{87}Sr/^{86}Sr$ values of 0.7037–0.7041 and $\varepsilon_{Nd}(t)$ values of +4.2 to +5.1, and yield young single-stage Nd model ages (T_{DM1}[Nd]) of 0.65–0.57 Ga.

Mineral Compositions

Major element compositions of amphibole from the Nyemo plutons, Renbu plutons, and Xigaze plutons are shown in Figure 8 and listed in Table S6 (see footnote 1). Calcic amphiboles within the felsic rocks and MMEs have distinct major element compositions and define trends of increasing bulk-rock silica content. Amphiboles in the felsic rocks are magnesiohornblende and ferrotschermakite (Fig. 8A; Leake et al., 1997); those in the MMEs are magnesiohornblende and tremolite (Fig. 8A). Amphiboles in felsic rocks have lower MgO contents and higher FeO, Al_2O_3, and Cl contents than the amphibole in the MMEs (Figs. 8B–8D). Amphibole Mg numbers, with Mg# = molar (100*Mg/ [Mg + Fe]), of the felsic rocks range from 0.44 to 0.63 for Nyemo plutons and 0.45–0.59 for Renbu plutons, which is slightly lower than those of the MMEs (0.52–0.71 for Nyemo plutons and 0.53–0.60 for Renbu plutons).

DISCUSSION

Petrogenesis of the Mafic Magmatic Enclaves

Late Cretaceous (ca. 90–85 Ma) intrusive rocks are widely exposed in the Gangdese batholith. The lithologies include gabbro, gabbroic diorite, diorite, monzonite, quartz diorite, and granodiorite with high-K calc-alkaline and metaluminous (A/CNK = 0.65–0.96) signatures (Fig. 4). The main exposures of Late Cretaceous intrusive rocks of the Nyemo plutons, Renbu plutons, and Xigaze plutons are adakitic granitoids that exhibit high K_2O contents, Sr/Y, and La/Yb ratios (Figs. 6A and 6B). They are distinct from contemporaneous slab-derived, sodium-rich adakites in the Lhasa terrane (ca. 90–85 Ma) (Fig. 4B; Zhang et al., 2010; Yin et al., 2020). The mechanisms enabling the generation of coeval calc-alkaline rocks and adakite in the Gangdese batholith remain poorly understood.

Several genetic models have been proposed for the genesis of the Gangdese batholith. These include combinations of (1) partial melting of the continental lower crust (Wen et al., 2008; Ji et al., 2014); (2) partial melting of the subducting oceanic crust (Zhang et al., 2010; Ma et al., 2013a, 2013b); (3) fractional crystallization of

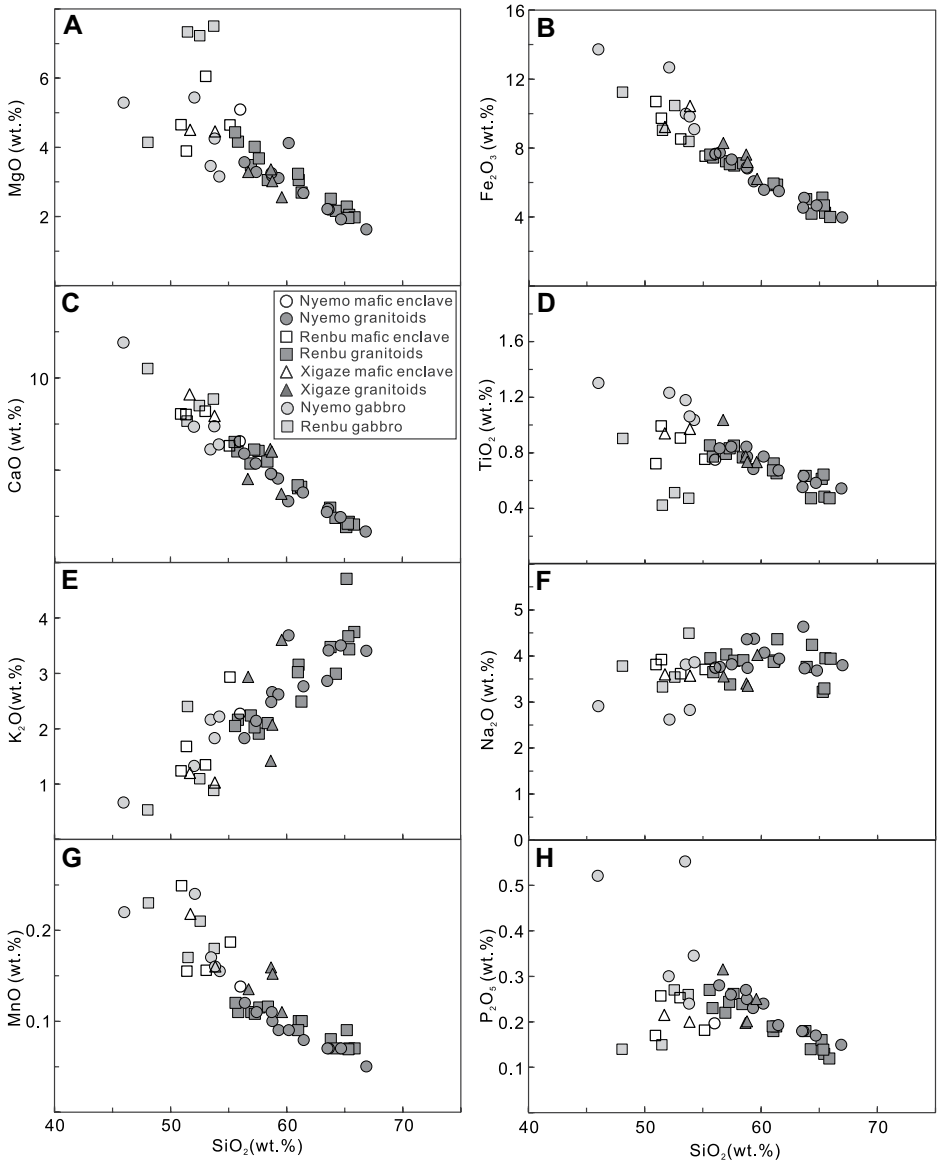

Figure 5. Harker diagrams illustrate the different fractionation trends for the Nyemo plutons, Renbu plutons, and Xigaze plutons.

basaltic arc-type lavas (Xu et al., 2015); and (4) magma mixing of slab-derived melts with melts formed from the mantle wedge (Ma et al., 2017). An integrated petrogenetic model is presented here to elucidate the genetic link responsible for forming the diverse lithological and mineral characteristics of plutonism in the southern Lhasa subterrane.

The ca. 90–85 Ma intrusive rocks in the Gangdese batholith represent a continuous gabbroic to granodioritic magmatic suite (Fig. 4A). The mafic rocks in the Nyemo plutons, Renbu plutons, and Xigaze plutons occur as MMEs within the host granitoid. Three main models have been proposed to explain the generation of MMEs hosted in granitoids, including restites after partial melting, autoliths formed by crystal-liquid separation, and hybrids of magma hybridization during mechanical mixing (e.g., Vernon, 1984; Dodge and Kistler, 1990; Didier and Barbarin, 1991; Wiebe et al., 1997; Weinberg et al., 2021). A wall-rock or restite origin for the MMEs in the Gangdese batholith can be precluded for the following reasons. The MMEs are ellipsoidal, spindle-shaped, or subangular and exhibit typical fine-grained, equigranular magmatic textures rather than those of metamorphic or residual sedimentary fabrics (Fig. 2). In addition, MMEs as wall-rock or restite origin should be older than their host rocks, but instead the crystallization ages of the MMEs and host granitoids overlap within uncertainty.

MMEs do not display characteristics of crystal cumulates either. (1) The absence of biotite-rich rinds and accumulate texture of the enclaves studied does not support cognate origin. (2) The chondrite-normalized REE patterns of the MMEs and host granitoids almost overlap with one another and exhibit similar Eu anomalies. If the MMEs were formed by accumulation, distinct REE patterns would have been observed. In particular, LREEs are largely incompatible elements in rock-forming minerals (e.g., plagioclase, clinopyroxene, and amphibole) during magma differentiation (Dai et al., 2017), which implies that fractionation of these minerals would have caused an enrichment in LREEs and negative Eu anomalies in the residual felsic magmas. Segregation of LREE-rich accessory minerals (e.g., titanite) would not significantly change the REE patterns of the MMEs, since this process usually occurs in silicic magmas rather than in mafic melts (Bea, 1996).

The presence of mineral textures indicative of disequilibrium (e.g., biotite mantled by amphibole and amphibole mantled by clinopyroxene) and rapid cooling (e.g., acicular apatites; Fig. 2) further indicates that MMEs were more likely to have formed via magma mingling and represent the extraneous globules of a mafic magma entrained into felsic magma chambers (Sparks and Marshall, 1986; Słaby and Martin, 2008). This interpretation is further supported by the correlations among SiO_2 and major oxides for the MMEs and the host granitoids (Fig. 5), which indicate a binary mixing pattern (Dodge and Kistler, 1990).

The geochemical and isotopic characteristics of the MMEs provide clues to the magma origin of the Gangdese batholith. The depletion of Nb, Ta, Zr, Hf, and Ti and enrichment of LREE (Fig. 7) of the MMEs suggests a distinctive origin relative to common arc magmas (Kelemen et al., 2003) and the continental crust generally (Rudnick and Gao, 2003). The positive whole-rock $\varepsilon_{Nd}(t)$ values (+4.2 to +5.1) and zircon $\varepsilon_{Hf}(t)$ values (+11.9 to +13.8; Fig. 9) are consistent with their origin from a mantle source, possibly with contributions from a fluid of the slab or via crustal contamination (Ma et al., 2015; Xu et al., 2019).

The following lines of evidence allow us to elucidate that the derivation of metasomatized, mantle-derived magmas was responsible for the origin of the MMEs. All MMEs display a range of Ba/La, Th/Yb, and Nb/Yb ratios (Fig. 10) that is consistent with generation from a subduction-modified mantle source (Pearce, 2014; Chapman and Clarke, 2021). These enriched characteristics of mantle-derived rocks probably result from the contribution of slab-derived fluids or melts during the subduction of the Neo-Tethys

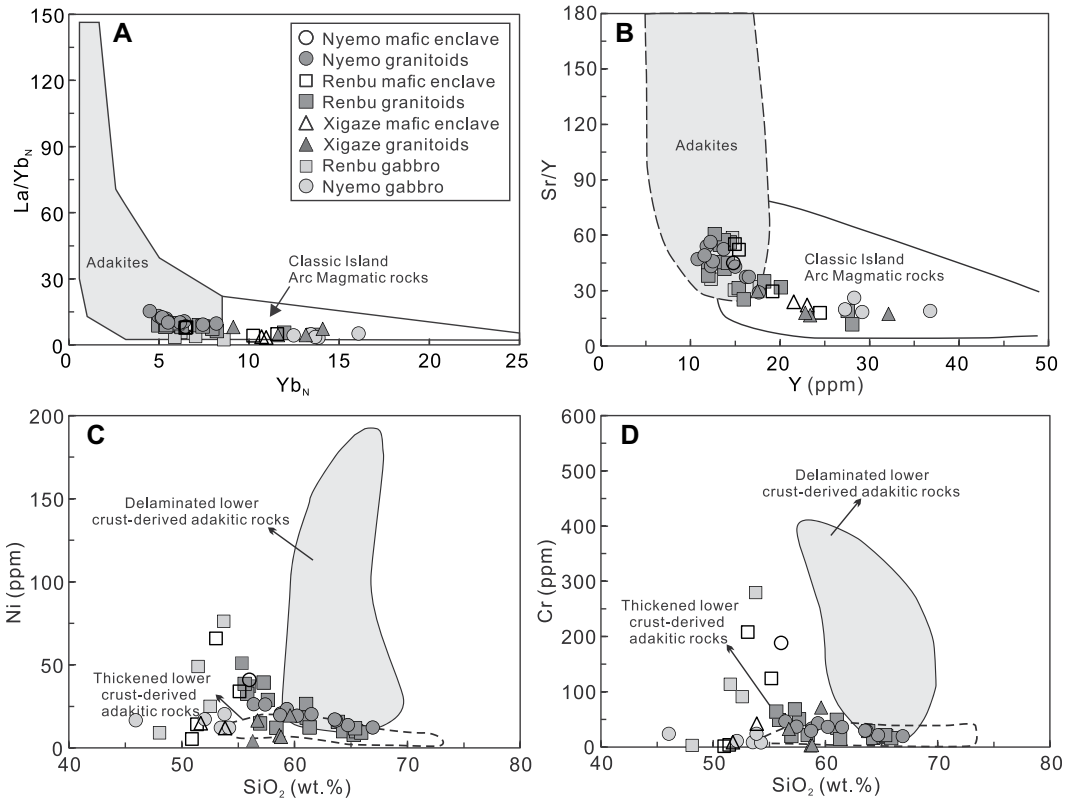

Figure 6. Major and trace element diagrams are shown for the Nyemo plutons, Renbu plutons, and Xigaze plutons from the Gangdese batholith. (A) Yb_N versus $(La/Yb)_N$; (B) Y versus Sr/Y; (C) SiO_2 versus Ni; (D) SiO_2 versus Cr. Fields of adakitic rocks and arc magmatic rocks are after Defant and Drummond (1990) and Martin et al. (2005). Fields of delaminated lower crust-derived and thick lower crust-derived adakitic rocks were constructed using the compilations of Wang et al. (2006).

oceanic slab. While it is generally believed that the depleted Nd–Sr–Hf isotopic compositions of the MMEs are consistent with an asthenospheric mantle (Ji et al., 2014), the MMEs studied exhibit enrichment in LREEs and LILEs and depletion in HFSEs (Fig. 7), which indicates a different mantle end-member or more involvement of enriched materials. The lower Nb/U (3.51–18.37), Ce/Pb (5.01–12.22), and Nb/La (0.22–0.48) ratios of the MMEs as compared with those of mid-oceanic-ridge basalt (MORB) and oceanic-island basalt (OIB) with consistent Nb/U ratios of 47 ± 10, Ce/Pb ratios of 25 ± 5, and Nb/La ratios >1 (Hofmann et al., 1986; Bradshaw and Smith, 1994; Smith et al., 1999) imply a depleted subcontinental lithospheric mantle source rather than an asthenospheric mantle source.

Primary magmas generated by partial melting of the lithospheric mantle generally occur at great depth in the stability fields of garnet or spinel, which can be identified by middle rare earth element (MREE)/HREE ratios (Karsli et al., 2017). Both the MMEs and coeval gabbro exhibit negatively inclined MREE to HREE patterns (Fig. 7) with Gd/Yb ratios of 1.5–2.5 and 1.6–2.9, respectively which indicates melting of the spinel-bearing mantle sources. Meanwhile, the MMEs plot along a mantle array and the modeling results imply that low portions (~1%–8%) of partial melting of a spinel-bearing mantle is consistent with the generation of those samples (Fig. 11A). To better constrain the source mineralogy and mantle melting history of the MMEs, we performed a non-modal batch melting modeling experiment (Shaw, 2000) to quantify the degree of melting (Fig. 11B). Model parameters, partition coefficients, and all calculations are provided in Table S7 (see footnote 1). The model results show that the REE pattern of the MME parental magma is best reproduced by a low degree (F = 0.05) of melting of a spinel lherzolite (2% spinel), using a depleted MORB mantle (DMM) with 10% altered oceanic crust (AOC) melt as the magma source. Therefore, we propose that the precursor magma of the enclaves was produced by partial melting of the depleted lithospheric mantle (spinel-bearing lherzolite) that was metasomatized by slab-derived fluids.

Genetic Link between the Mafic Enclave and Their Host Felsic Rocks

The origin of felsic magmas in arc settings has been attributed to a combination of two main processes: (1) derivation from a primary basaltic magma, or (2) partial melting of a previous crustal rock (Chappell et al., 1987; Annen et al., 2006; Bachmann and Huber, 2019). Additionally, crustal assimilation involving mixing of melts from diverse sources has been suggested in different studies (Hildreth and Moorbath, 1988; Xu et al., 2019). Large-scale magma mixing between mantle- and crust-endmember components to generate intermediate compositions is not realistic here, as detailed geochemical and isotopic compositions obtained for coeval intrusion (Fig. 1B) have convincingly shown that magma mixing was inefficient in these magmas (Zhang et al., 2010; Xu et al., 2015; Guo et al., 2020; Wang et al., 2021). Thus, we focus our attention on models of fractional crystallization and partial melting.

The widespread MMEs in granitoids are generally considered to be petrological evidence of the formation of host magmas via extensive differentiation of basaltic magma, for which the MMEs represent early crystallized cumulates. In the SiO_2 variation diagrams (Figs. 4A–4C and 5), virtually all major elements show correlations with SiO_2 contents from granitoids. For example, MgO, $Fe_2O_3^T$, CaO, TiO_2, and MnO decrease with increasing SiO_2, whereas $Na_2O + K_2O$, K_2O, and $Na_2O + K_2O$–CaO increase with increasing SiO_2. Such correlations could be controlled by either fractional crystallization, magma mixing, or partial melting. However, in the diagrams of La versus $(La/Sm)_N$ and Th versus Th/Nd (Fig. 12), the granitoids plot along the partial melting/magma mixing trend rather than the fractional crystallization trend. Therefore, fractional crystalliza-

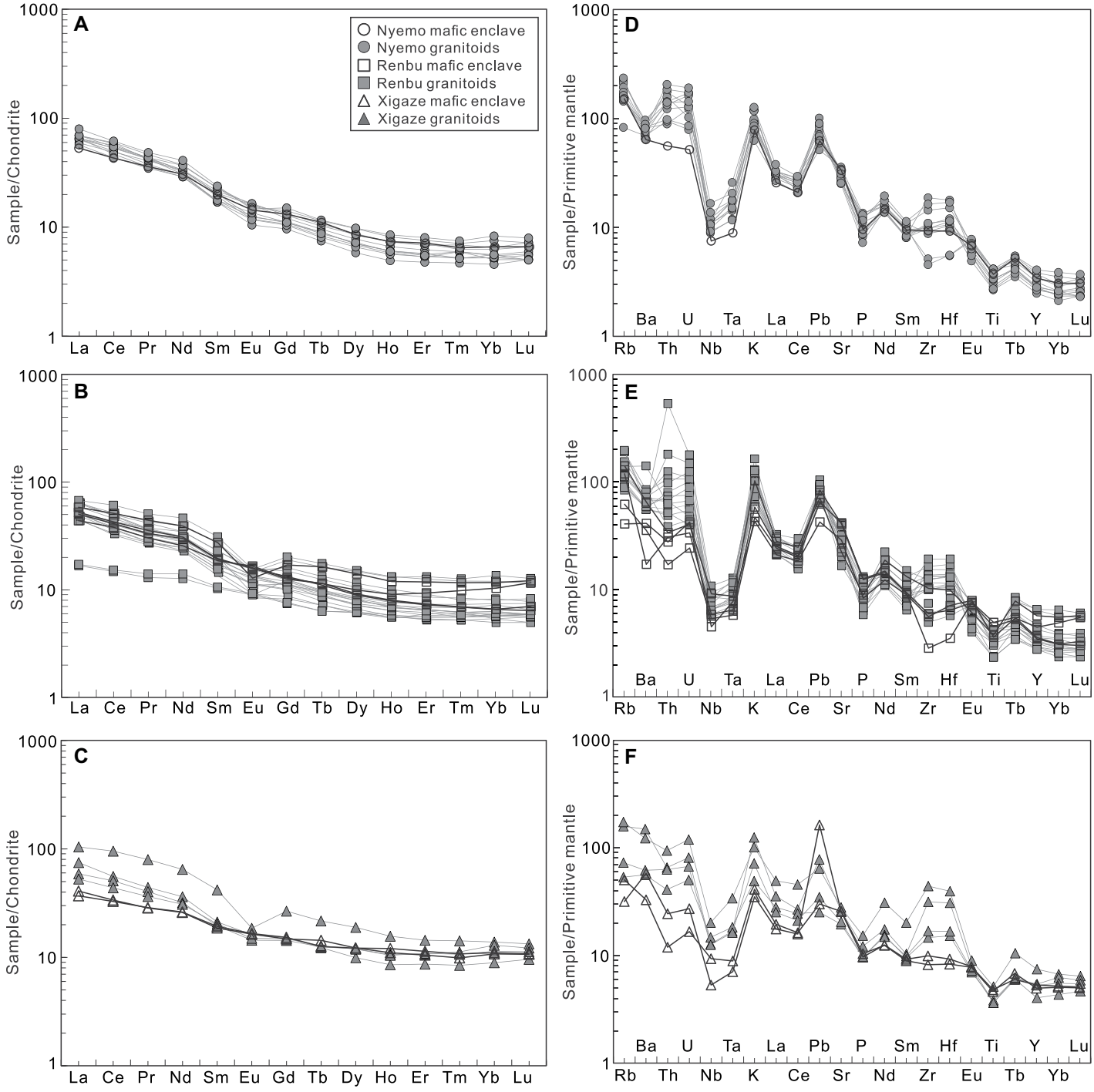

Figure 7. Chondrite-normalized rare earth element patterns (A, B, and C) and primitive mantle-normalized trace-element diagrams (D, E, and F) for the Nyemo plutons, Renbu plutons, and Xigaze plutons from the Gangdese batholith are shown. Chondrite and primitive mantle values used for normalization are from Boynton (1984) and McDonough and Sun (1995), respectively.

tion does not account for the petrogenesis of these granitoids.

Most of the granitoids in the Nyemo plutons, Renbu plutons, and Xigaze plutons are metaluminous (A/CNK < 1.1) and Na-rich (only two granite samples have $Na_2O/K_2O < 1.1$). Na-rich granitic magma could originate from H_2O-fluxed melting of metapelite at high pressure (~10 kbar; Patiño Douce and Harris, 1998) or the partial melting of metabasic rock such as amphibolite (Richards and Kerrich, 2007). All of the granitoids are metaluminous, with low Rb/Sr and Rb/Ba ratios and high MgO and $Fe_2O_3^T$ contents, which are distinct from metapelite-derived melts (Rong et al., 2017). Moreover, the adakitic geochemical characteristics of the granitoids studied that have weak to negative Eu anomalies (Eu* = 0.56–1.02; Table S4) are

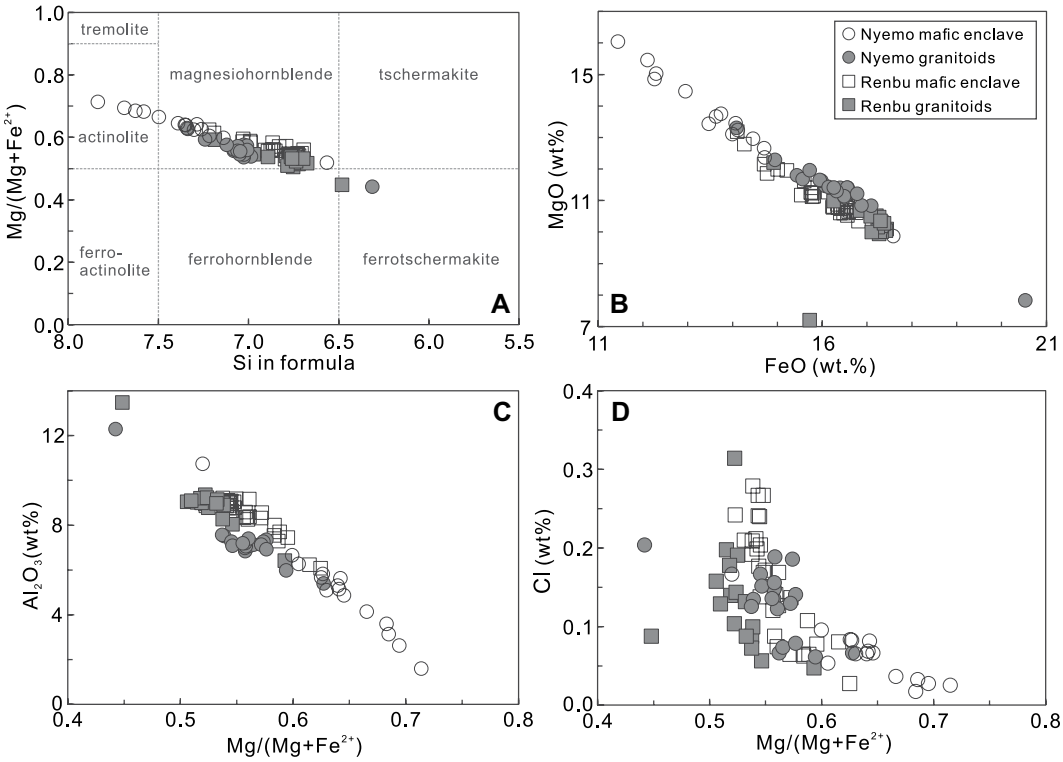

Figure 8. Major element compositions of amphiboles from the study area are plotted. (A) Classification of calcic amphibole using the diagram outlined by Leake et al. (1997) as follows: $Ca_B \geq 1.50$, $(Na + K)_A \geq 0.50$, and $Ca_A < 0.50$, (B) FeO versus MgO, (C) $Mg/(Mg + Fe^{2+})$ versus Al_2O_3, and (D) Cl versus $Mg/(Mg + Fe^{2+})$ versus Cl. Note that phenocrystic Amp within the granitoid has more evolved compositions than the mafic enclaves.

consistent with the partial melting of garnet-bearing amphibolite, eclogite, and oceanic slab. Furthermore, compared with the coeval slab-derived, sodium-rich adakites in the Gangdese batholith, the adakite-like granitoids studied, as a whole, have significantly higher SiO_2 and K_2O contents (Fig. 4B). This suggests that the granitoids studied were derived from partial melting of the thickened lower crust. The granitoids in the Nyemo plutons, Renbu plutons, and Xigaze plutons are enriched in LILEs (Th, U, K, and Pb) and LREEs and depleted in HFSEs (Nb, Ta, Ti, and P; Fig. 7), similar to the continental crust. In the $(^{87}Sr/^{86}Sr)_i$ versus $\varepsilon_{Nd}(t)$ diagram (Fig. 9A), isotopic compositions of Mesozoic to Cenozoic granitic rocks in the Gangdese batholith are plotted for comparison (Ma et al., 2013a, 2013b; Jiang et al., 2012; Yin et al., 2020; Wang et al., 2021). The granitoid of the Nyemo plutons, Renbu plutons, and Xigaze plutons, similar to coeval granitoids in the Gangdese

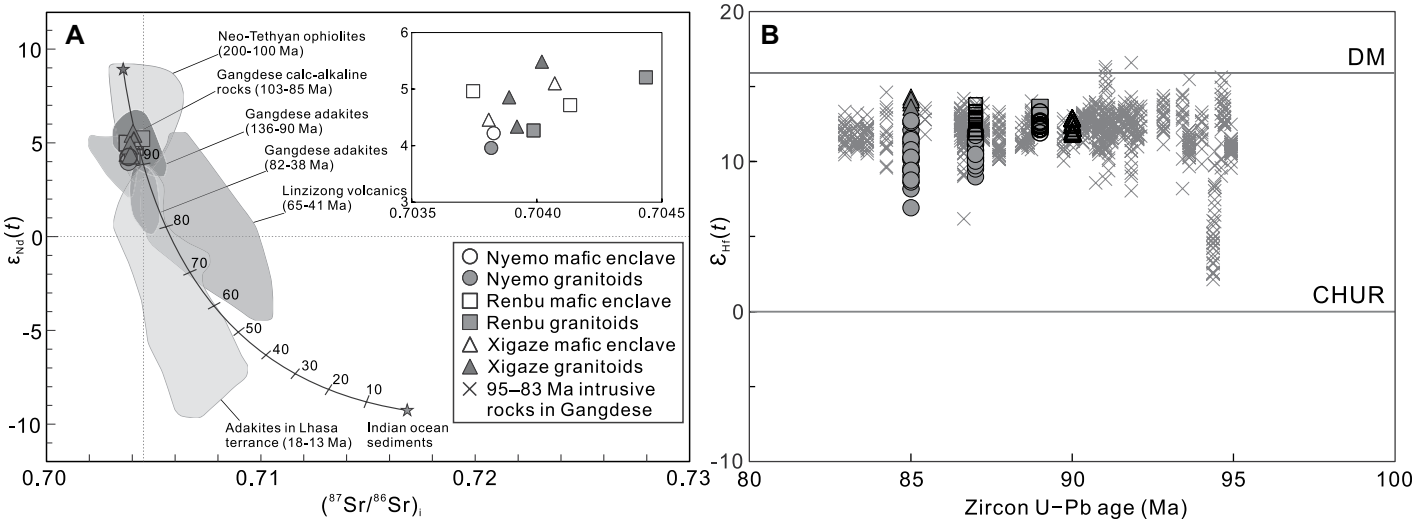

Figure 9. (A) Whole-rock initial $(^{87}Sr/^{86}Sr)_i$ versus $\varepsilon_{Nd}(t)$ and (B) zircon U–Pb age versus $\varepsilon_{Hf}(t)$ diagrams are shown for the Nyemo plutons, Renbu plutons, and Xigaze plutons from the Gangdese batholith. Data sources: Yarlung Tsangpo ophiolites: Xu and Castillo (2004); Zhang et al. (2005); Gangdese calc-alkaline rocks: Wen et al. (2008); Linzizong volcanic rocks: Mo et al. (2007, 2008); post-collisional adakites in the Lhasa Block (18–13 Ma): Guo et al. (2007); Hou et al. (2004). Data sources from the literature for intrusive rocks in the Gangdese batholith dated from 90 Ma to 85 Ma are in Table S1 (see text footnote 1).

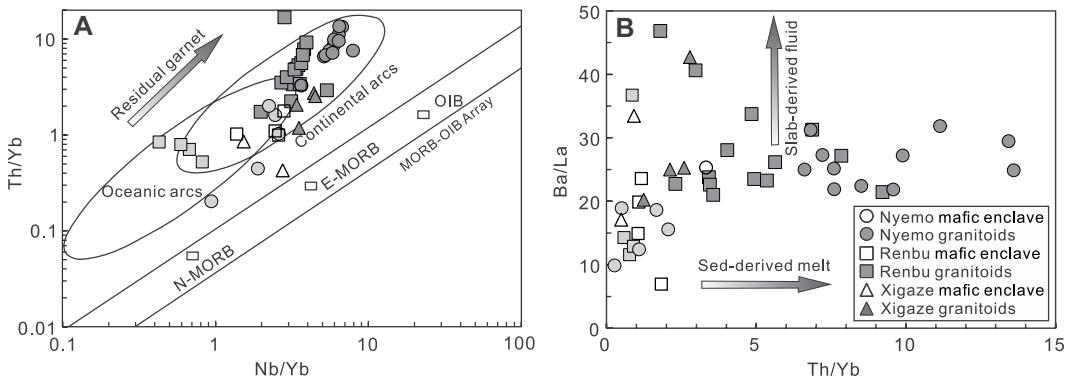

Figure 10. (A) Nb/Yb versus Th/Yb diagram (Pearce, 2014) and (B) Th/Yb versus Ba/La diagram for the Nyemo plutons, Renbu plutons, and Xigaze plutons are shown.

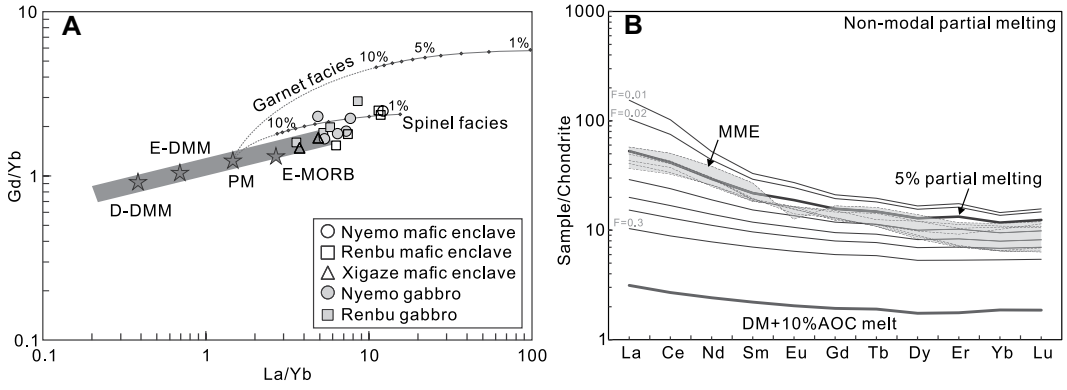

Figure 11. (A) A variation diagram plots La/Yb versus Gd/Yb for the mafic enclave samples. Chondrite normalized rare earth element plots for mafic magmatic enclaves (MMEs) show (B) non-modal partial melting model (black line). Chondrite normalizing values and average enriched mid-oceanic-ridge basalt (E-MORB) are from Sun and McDonough (1989). Also shown are primitive mantle (PM; Palme and O'Neill, 2004), depleted MORB mantles and enriched-depleted MORB mantles (D-DMM and E-DMM, respectively; Workman and Hart, 2005) to demonstrate the mantle array (gray field). Mineral and melt modes for spinel- and garnet-facies mantle mineralogy are ol0.53(−0.06) + opx0.27(0.28) + cpx0.17(0.67) + sp0.03(0.11) (Kinzler, 1997) and ol0.60(0.03) + opx0.20(−0.16) + cpx0.10(0.88) + gt0.10(0.09) (Walter, 1998), respectively. Melting curves with increments of 1%–10% were calculated using the non-modal fractional melting equation of Shaw (1970). The partition coefficients are from Adam and Green (2006).

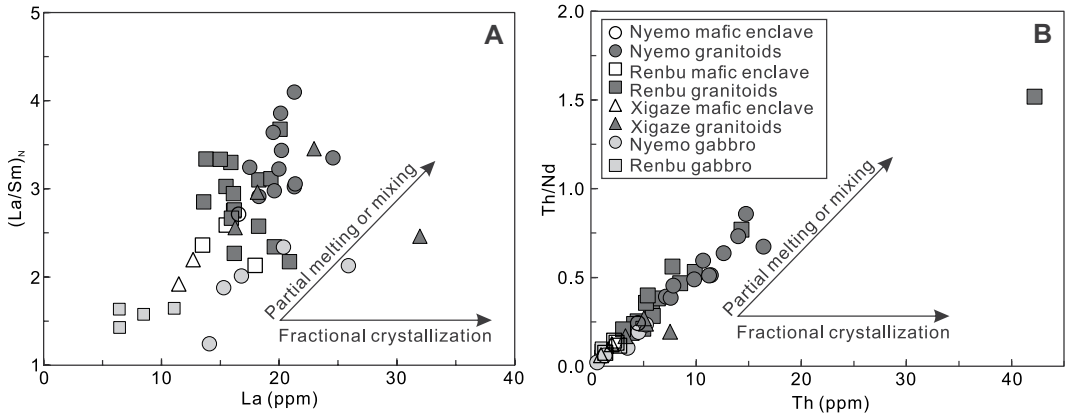

Figure 12. Diagrams show (A) whole-rock La contents versus $(La/Sm)_N$ ratios and (B) Th contents versus Th/Nd ratios for the Nyemo plutons, Renbu plutons, and Xigaze plutons.

batholith but lower than Neo-Tethyan ophiolites, have depleted isotopic compositions with the $(^{87}Sr/^{86}Sr)_i$ of most samples ranging from 0.702 to 0.704, with positive $\varepsilon_{Nd}(t)$ (+4.95 to +6.50) and $\varepsilon_{Hf}(t)$ (+6.14 to +13.33; Fig. 9), which is consistent with these granitoids being derived from lower continental crust rather than the subducted slab.

Construction of the Transcrustal Magmatic System

Models for the generation of granitic magma within the crust involve partial melting of the pre-existing crust (Chappell et al., 1987) and/or derivation of mantle-derived basaltic magmas in the deep crustal hot zone (Annen et al., 2006; Davidson et al., 2007). Underplating or flux of mafic magma may play a major role in driving the differentiation of high-silica compositions by reactivating magma reservoirs (Bachmann and Bergantz, 2004). The extensive exposure of mafic enclaves within the Nyemo plutons, Renbu plutons, and Xigaze plutons as well as within coeval plutons is direct evidence of their

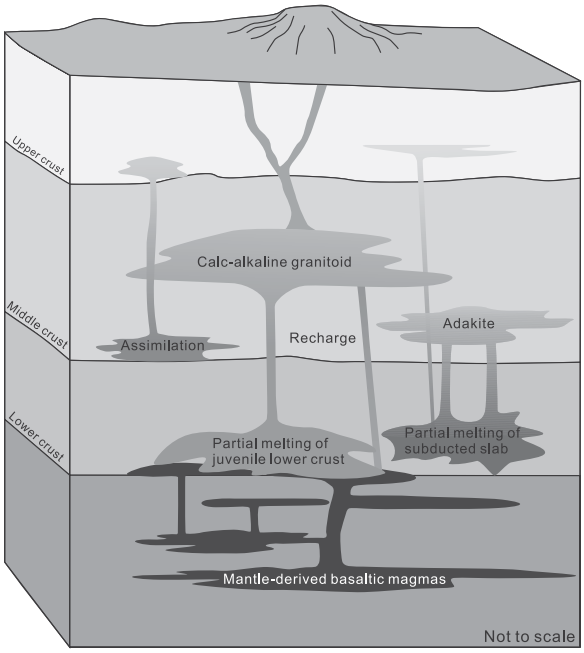

Figure 13. Schematic model shows the Gangdese transcrustal magmatic system in which the magmas represented by the rock assemblages described in this study were generated. The successive under-plating or intra-plating of mantle-derived basaltic magmas formed deep crustal hot zones in which partial melting of the juvenile crust and fractional crystallization and replenishment of primitive mafic magma occurred at various depths. The different shades of gray represent probable crustal compositions due to magmatic differentiation.

replenishment and the interaction between the mantle-derived and crust-derived magmas beneath the Gangdese batholith. Amphiboles are common hydrous minerals in magmatic rocks and particularly in those arc-related rocks. Amphibole textures and compositions therefore have been utilized to decipher magmatic processes and crystallization conditions (Chelle-Michou and Chiaradia, 2017; Davidson et al., 2007). Amphiboles from the MMEs and granitoids are characterized by different compositional trends in both Nyemo plutons and Renbu plutons, which indicates that they crystallized from the different host magmas (Fig. 8). Meanwhile, a negative correlation between Al_2O_3 and Mg# in the amphibole crystals (Fig. 8C) indicates that mafic magma replenishment plays a significant role in the petrogenesis of these plutons (Kiss et al., 2014; Ridolfi et al., 2010). If the amphibole chemistry of MMEs in the different plutons is taken as a proxy for melt evolution, then the Nyemo plutons, Renbu plutons, and Xigaze plutons evolved from the different magmatic systems, which is indicative of episodic mafic injection. The large magma bodies could have been generated by partial melting of the mafic lower crust, which is continually heated by a periodic influx of basaltic magma (Petford and Gallagher, 2001).

Taken together, a plausible petrogenetic model is proposed in which multiple magma reservoirs and magma recharge events at various crustal levels led to the formation of the Gangdese batholith (Fig. 13). Initially, partial melting of metasomatized lithospheric mantle generated basaltic magmas that underplated at the mantle–crust interface (Fig. 13). Subsequently, the calc-alkaline granitoids were generated by partial melting of the mafic lower continental crust, whereas the coeval adakites were derived from partial melting of the subducted oceanic crust (Fig. 13). Finally, replenishment of the mantle-derived basaltic magmas led to the formation of enclave-bearing granitoids, as represented by the Nyemo plutons, Renbu plutons, and Xigaze plutons in the Gangdese batholith (Fig. 13).

Crustal Thickening in Late Cretaceous

The thick crust and high elevation of the present-day Tibetan Plateau are commonly attributed to the Cenozoic collision of India with Asia (Turner et al., 1993; Chung et al., 1998; Zhu et al., 2017). Previous studies suggested that the Late Cretaceous granitoids might have been generated by melting of the oceanic slab or seamount (Zhu et al., 2013, 2017), and hence the geochemical proxies are not considered valid for reconstructing crustal thickness. However, increasing regional geological observations are consistent with the crust of southern Tibet having been thickened since the Late Cretaceous. These include a transition in sedimentation from shallow marine limestones of the Takena Formation to clastic sediments at the base of the Shexing Formation in the Linzhou Basin, which reflects the onset of topographic growth and crustal thickening of the southern Lhasa terrane (Leier et al., 2007b; Wang et al., 2020). In addition, interformational structural relationships are consistent with the Takena Formation experiencing contractional deformation during the Late Cretaceous, which involved at least 26%–50% of the north–south shortening in the Lhasa terrane (Burg et al., 1983; Kapp et al., 2005; Leier et al., 2007a). Detailed studies of the Al-in-hornblende barometry reveal the exhumation history of the Gangdese batholith, and the middle- to lower-crustal rocks show progressive burial from 20 km to 40 km during the Late Cretaceous (ca. 95–72 Ma; Cao et al., 2020). The country rocks of the Gangdese batholith record high-pressure granulite-facies metamorphism at ca. 87–89 Ma that is consistent with burial to depths of up to 55 km (Ding et al., 2022; Zhang et al., 2022). Detrital zircons separated from modern river sands in the Gangdese belt reveal two episodes of crustal thickening (to 60–70 km) during the Late Cretaceous and early Cenozoic (Fig. 14A; Tang et al., 2021).

The Late Cretaceous subduction-related intermediate to felsic rocks in the southern Lhasa terrane provide additional constraints on the crustal thickness of the region. The granitoids studied show adakitic signatures but with higher K_2O contents than coeval subducted, slab-derived adakites (Fig. 4B; Zhang et al., 2010; Jiang et al., 2012), which indicates that they originated from thickened lower crust. The Sr/Y and La/Yb ratios of intermediate–felsic igneous rocks in continental arcs correlate well with crustal thickness at global and regional scales (Chapman et al., 2015; Profeta et al., 2015). The ratio of Sr to Y is a commonly used geochemical index for tracking changes in the Cretaceous crustal thickness of the southern Lhasa terrane. The $(La/Yb)_N$ and Sr/Y ratios of granitoids in this study, combined with a compiled data set of magmatic rocks from the southern Lhasa terrane, indicate that the crustal thickness of the southern Lhasa terrane started at ~40 km during the Early Cretaceous and early Cenozoic (Fig. 14). A gradual increase to an average thickness of ~50 km occurred in the Late Cretaceous (Figs. 14B and 14C). Previous studies have suggested that the incompatible element abundances of the arc have shown a strong correlation with the crustal thickness (i.e., Moho depth). Turner and Langmuir (2015) reconstructed global arc crustal thickness based on MREE/HREE ratios (i.e., Dy/Yb) of arc magmatic rocks. All Late Cretaceous magmatic rocks studied here show a similar steep slope going from LREE to HREE to that of the arc samples in the Southern Volcanic Zone of Chile and in Central America, which exhibit consistent and high Dy/Yb ratios (1.5–2.1 for the MMEs and 1.4–2.2 for the granitoid). This suggests that the Late Cretaceous magmatic rocks in the Gangdese batholith are produced through the limited crustal melting in a thick-crusted arc (45–50 km), resembling volcanic rocks in the Popocatepetl and Don Casimiro

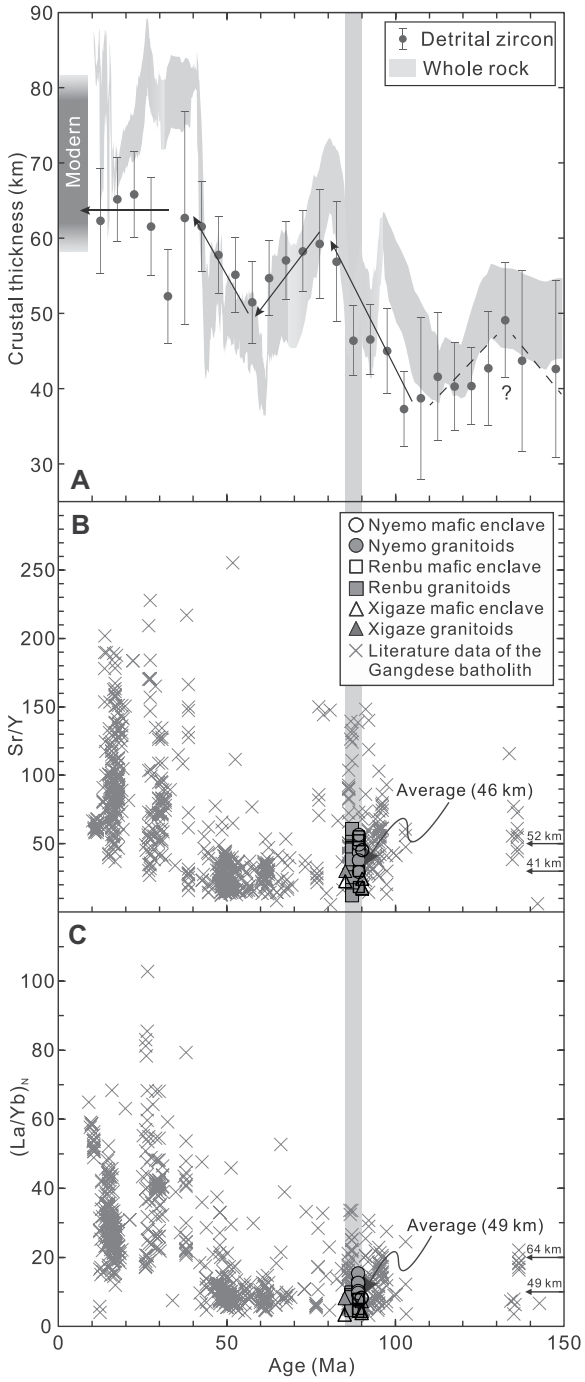

Figure 14. Graphs plot the evolution of crustal thickness of the Gangdese magmatic belt, southern Tibet. (A) Crustal thickness reconstructed from Eu/Eu* [Eu/Eu* = Eu_N / $(Sm_N \times Gd_N)^{0.5}$] in detrital zircons (Tang et al., 2021). (B and C) Crustal thickness calculated using the whole-rock (B) Sr/Yb and (C) La/Yb methods (Sundell et al., 2021). Gangdese whole-rock La/Yb data are from Chapman and Kapp (2017) and Table S1 (see text footnote 1).

volcanoes (Turner and Langmuir, 2022). Our results, combined with existing data, indicate that Late Cretaceous (ca. 90–85 Ma) subduction prior to Indo-Asia collision might have played an important role in the thickening of the southern Lhasa terrane.

CONCLUSIONS

Field and petrological observations show that the Late Cretaceous batholiths in the Gangdese are mainly composed of enclave-bearing granitoids. Both MMEs and granitoids crystallized between 90 Ma and 85 Ma. Geochemical and isotopic data suggest that the MMEs were derived from the partial melting of a depleted mantle component with a contribution from the subduction-related materials. The granitoids were generated by partial melting of juvenile crust. The underplating and replenishing of mantle-derived magmas could have supplied sufficient heat to trigger melting of the thickened crust that led to the construction of enclave-bearing granitoids in the Nyemo plutons, Renbu plutons, and Xigaze plutons. In this context, contrasting origins could reflect the evolution of crustal thickness. Our results reveal that the crust was thickened to ~50 km during the Late Cretaceous (ca. 90–85 Ma) in advance of the Cenozoic Indo-Asia collision.

ACKNOWLEDGMENTS

This work was supported by the National Natural Science Foundation of China (grant nos. 41888101 and 41572041). T. Chapman acknowledges support from the University of New England. We thank Jian-Sheng Qiu and Hang Xu for their assistance in the field and De-Hong Du for the discussion. This paper benefitted from constructive comments by Lorenzo Tavazzani and an anonymous reviewer as well as editorial handling by science editor Wenjiao Xiao and associate editor Shan Li.

REFERENCES CITED

Adam, J., and Green, T., 2006, Trace element partitioning between mica-and amphibole-bearing garnet lherzolite and hydrous basanitic melt: 1. Experimental results and the investigation of controls on partitioning behaviour: Contributions to Mineralogy and Petrology, v. 152, p. 1–17, https://doi.org/10.1007/s00410-006-0085-4.

Alasino, P.H., Paterson, S.R., Kirsch, M., and Larrovere, M.A., 2022, The role of crustal thickness on magma composition in arcs: An example from the pre-Andean, South American Cordillera: Gondwana Research, v. 106, p. 191–210, https://doi.org/10.1016/j.gr.2022.01.009.

Allègre, C.J., and Othman, D.B., 1980, Nd–Sr isotopic relationship in granitoid rocks and continental crust development: A chemical approach to orogenesis: Nature, v. 286, p. 335–342, https://doi.org/10.1038/286335a0.

Andersen, T., 2002, Correction of common lead in U–Pb analyses that do not report ^{204}Pb: Chemical Geology, v. 192, no. 1–2, p. 59–79, https://doi.org/10.1016/S0009-2541(02)00195-X.

Annen, C., Blundy, J., and Sparks, R., 2006, The genesis of intermediate and silicic magmas in deep crustal hot zones: Journal of Petrology, v. 47, no. 3, p. 505–539, https://doi.org/10.1093/petrology/egi084.

Ardill, K., Paterson, S., and Memeti, V., 2018, Spatiotemporal magmatic focusing in upper-mid crustal plutons of the Sierra Nevada arc: Earth and Planetary Science Letters, v. 498, p. 88–100, https://doi.org/10.1016/j.epsl.2018.06.023.

Bachmann, O., and Bergantz, G., 2004, On the origin of crystal-poor rhyolites: Extracted from batholithic crystal mushes: Journal of Petrology, v. 45, p. 1565–1582, https://doi.org/10.1093/petrology/egh019.

Bachmann, O., and Huber, C., 2019, The inner workings of crustal distillation columns; the physical mechanisms and rates controlling phase separation in silicic magma reservoirs: Journal of Petrology, v. 60, p. 3–18, https://doi.org/10.1093/petrology/egy103.

Bachmann, O., Miller, C.F., and de Silva, S.L., 2007, The volcanic–plutonic connection as a stage for understanding crustal magmatism: Journal of Volcanology and Geothermal Research, v. 167, p. 1–23, https://doi.org/10.1016/j.jvolgeores.2007.08.002.

Barbarin, B., 2005, Mafic magmatic enclaves and mafic rocks associated with some granitoids of the central Sierra Nevada batholith, California: Nature, origin, and relations with the hosts: Lithos, v. 80, no. 1–4, p. 155–177, https://doi.org/10.1016/j.lithos.2004.05.010.

Bateman, P.C., 1992, Plutonism in the central part of the Sierra Nevada batholith, California: U.S. Geological Survey Professional Paper 1483, 186 p.

Bateman, P.C., and Chappell, B.W., 1979, Crystallization, fractionation, and solidification of the

Tuolumne intrusive series, Yosemite National Park, California: Geological Society of America Bulletin, v. 90, p. 465–482, https://doi.org/10.1130/0016-7606(1979)90<465:CFASOT>2.0.CO;2.

Bea, F., 1996, Residence of REE, Y, Th and U in granites and crustal protoliths; implications for the chemistry of crustal melts: Journal of Petrology, v. 37, p. 521–552, https://doi.org/10.1093/petrology/37.3.521.

Bergantz, G.W., 1989, Underplating and partial melting: Implications for melt generation and extraction: Science, v. 245, p. 1093–1095, https://doi.org/10.1126/science.245.4922.1093.

Black, L.P., and Gulson, B.L., 1978, The age of the Mud Tank carbonatite, Strangways range, northern territory: BMR Journal of Australian Geology and Geophysics, v. 3, p. 227–232.

Blichert-Toft, J., and Albarède, F., 1997, The Lu–Hf isotope geochemistry of chondrites and the evolution of the mantle-crust system: Earth and Planetary Science Letters, v. 148, p. 243–258, https://doi.org/10.1016/S0012-821X(97)00040-X.

Blundy, J.D., and Sparks, R.S.J., 1992, Petrogenesis of mafic inclusions in granitoids of the Adamello Massif, Italy: Journal of Petrology, v. 33, p. 1039–1104, https://doi.org/10.1093/petrology/33.5.1039.

Boynton, W.V., 1984. Geochemistry of the rare earth elements: meteorite studies, *in* Henderson, P., ed., Rare Earth Element Geochemistry: Amsterdam, Elsevier, p. 63–114, https://doi.org/10.1016/B978-0-444-42148-7.50008-3.

Bradshaw, T.K., and Smith, E.I., 1994, Polygenetic Quaternary volcanism at Crater Flat, Nevada: Journal of Volcanology and Geothermal Research, v. 63, p. 165–182, https://doi.org/10.1016/0377-0273(94)90072-8.

Burg, J.P., Proust, F., Tapponnier, P., and Ming, C.G., 1983, Deformation phases and tectonic evolution of the Lhasa block (southern Tibet, China): Eclogae Geologicae Helvetiae, v. 76, p. 643–665.

Cao, W., Yang, J., Zuza, A.V., Ji, W.Q., Ma, X.X., Chu, X., and Burgess, Q.P., 2020, Crustal tilting and differential exhumation of Gangdese Batholith in southern Tibet revealed by bedrock pressures: Earth and Planetary Science Letters, v. 543, https://doi.org/10.1016/j.epsl.2020.116347.

Castro, A., Moreno-Ventas, I., and De La Rosa, J.D., 1991, H-type (hybrid) granitoids: A proposed revision of the granite-type classification and nomenclature: Earth-Science Reviews, v. 31, p. 237–253, https://doi.org/10.1016/0012-8252(91)90020-G.

Chapman, J.B., and Kapp, P., 2017, Tibetan magmatism database: Geochemistry, Geophysics, Geosystems, v. 18, p. 4229–4234, https://doi.org/10.1002/2017GC007217.

Chapman, J.B., Ducea, M.N., DeCelles, P.G., and Profeta, L., 2015, Tracking changes in crustal thickness during orogenic evolution with Sr/Y: An example from the North American Cordillera: Geology, v. 43, p. 919–922, https://doi.org/10.1130/G36996.1.

Chapman, T., and Clarke, G.L., 2021, Cryptic evidence for the former presence of lawsonite in blueschist and eclogite: Journal of Metamorphic Geology, v. 39, p. 343–362, https://doi.org/10.1111/jmg.12578.

Chapman, T., Clarke, G.L., and Daczko, N.R., 2016, Crustal differentiation in a thickened arc—evaluating depth dependences: Journal of Petrology, v. 57, p. 595–620, https://doi.org/10.1093/petrology/egw022.

Chappell, B.W., White, A.J.R., and Wyborn, D., 1987, The importance of residual source material (restite) in granite petrogenesis: Journal of Petrology, v. 28, p. 1111–1138, https://doi.org/10.1093/petrology/28.6.1111.

Chelle-Michou, C., and Chiaradia, M., 2017, Amphibole and apatite insights into the evolution and mass balance of Cl and S in magmas associated with porphyry copper deposits: Contributions to Mineralogy and Petrology, v. 172, p. 1–26, https://doi.org/10.1007/s00410-017-1417-2.

Chung, S.L., Lo, C.H., Lee, T.Y., Zhang, Y., Xie, Y., Li, X., Wang, K.L., and Wang, P.L., 1998, Diachronous uplift of the Tibetan plateau starting 40? Myr ago: Nature, v. 394, p. 769–773, https://doi.org/10.1038/29511.

Clemens, J.D., Elburg, M.A., and Harris, C., 2017, Origins of igneous microgranular enclaves in granites: The example of Central Victoria, Australia: Contributions to Mineralogy and Petrology, v. 172, p. 1–27, https://doi.org/10.1007/s00410-017-1409-2.

Dai, H.K., Zheng, J.P., Zhou, X., and Griffin, W.L., 2017, Generation of continental adakitic rocks: Crystallization modeling with variable bulk partition coefficients: Lithos, v. 272–273, p. 222–231, https://doi.org/10.1016/j.lithos.2016.12.020.

Davidson, J., Turner, S., Handley, H., Macpherson, C., and Dosseto, A., 2007, Amphibole "sponge" in arc crust?: Geology, v. 35, p. 787–790, https://doi.org/10.1130/G23637A.1.

Davies, J.H., and Stevenson, D.J., 1992, Physical model of source region of subduction zone volcanics: Journal of Geophysical Research: Solid Earth, v. 97, p. 2037–2070, https://doi.org/10.1029/91JB02571.

Defant, M.J., and Drummond, M.S., 1990, Derivation of some modern arc magmas by melting of young subducted lithosphere: Nature, v. 347, p. 662–665, https://doi.org/10.1038/347662a0.

Didier, J., and Barbarin, B., 1991, Enclaves and Granite Petrology: Elsevier, 625 p.

Ding, H., Zhang, Z., and Kohn, M.J., 2022, Late Cretaceous hydrous melting and reworking of juvenile lower crust of the eastern Gangdese magmatic arc, southern Tibet: Gondwana Research, v. 104, p. 112–125, https://doi.org/10.1016/j.gr.2021.07.017.

Dodge, F.C.W., and Kistler, R.W., 1990, Some additional observations on inclusions in the granitic rocks of the Sierra Nevada: Journal of Geophysical Research: Solid Earth, v. 95, p. 17,841–17,848, https://doi.org/10.1029/JB095iB11p17841.

Du, D.H., Wang, X.L., Wang, S., Miller, C.F., Xu, X., Chen, X., and Zhang, F.F., 2022, Deciphering cryptic multistage crystal-melt separation during construction of the Tonglu Volcanic–Plutonic Complex, SE China: Journal of Petrology, v. 63, https://doi.org/10.1093/petrology/egab098.

Ducea, M.N., Saleeby, J.B., and Bergantz, G., 2015, The architecture, chemistry, and evolution of continental magmatic arcs: Annual Review of Earth and Planetary Sciences, v. 43, p. 299–331, https://doi.org/10.1146/annurev-earth-060614-105049.

Farner, M.J., and Lee, C.T.A., 2017, Effects of crustal thickness on magmatic differentiation in subduction zone volcanism: A global study: Earth and Planetary Science Letters, v. 470, p. 96–107, https://doi.org/10.1016/j.epsl.2017.04.025.

Farner, M.J., Lee, C.T.A., and Mikus, M.L., 2018, Geochemical signals of mafic-felsic mixing: Case study of enclave swarms in the Bernasconi Hills pluton, California: Geological Society of America Bulletin, v. 130, p. 649–660, https://doi.org/10.1130/B31760.1.

Frost, B.R., Barnes, C.G., Collins, W.J., Arculus, R.J., Ellis, D.J., and Frost, C.D., 2001, A geochemical classification for granitic rocks: Journal of Petrology, v. 42, p. 2033–2048, https://doi.org/10.1093/petrology/42.11.2033.

Griffin, W.L., Pearson, N.J., Belousova, E., Jackson, S.V., Van Achterbergh, E., O'Reilly, S.Y., and Shee, S.R., 2000, The Hf isotope composition of cratonic mantle: LA-MC-ICPMS analysis of zircon megacrysts in kimberlites: Geochimica et Cosmochimica Acta, v. 64, p. 133–147, https://doi.org/10.1016/S0016-7037(99)00343-9.

Griffin, W.L., Wang, X., Jackson, S.E., Pearson, N.J., O'Reilly, S.Y., Xu, X., and Zhou, X., 2002, Zircon chemistry and magma mixing, SE China: In-situ analysis of Hf isotopes, Tonglu and Pingtan igneous complexes: Lithos, v. 61, p. 237–269, https://doi.org/10.1016/S0024-4937(02)00082-8.

Guo, L., Jagoutz, O., Shinevar, W.J., and Zhang, H.F., 2020, Formation and composition of the Late Cretaceous Gangdese arc lower crust in southern Tibet: Contributions to Mineralogy and Petrology, v. 175, p. 1–26, https://doi.org/10.1007/s00410-020-01696-y.

Guo, Z., Wilson, M., and Liu, J., 2007, Post-collisional adakites in south Tibet: Products of partial melting of subduction-modified lower crust: Lithos, v. 96, p. 205–224, https://doi.org/10.1016/j.lithos.2006.09.011.

Hildreth, W., 1981, Gradients in silicic magma chambers: Implications for lithospheric magmatism: Journal of Geophysical Research: Solid Earth, v. 86, p. 10,153–10,192, https://doi.org/10.1029/JB086iB11p10153.

Hildreth, W., and Moorbath, S., 1988, Crustal contributions to arc magmatism in the Andes of Central Chile: Contributions to Mineralogy and Petrology, v. 98, p. 455–489, https://doi.org/10.1007/BF00372365.

Hofmann, A.W., Jochum, K.P., Seufert, M., and White, W.M., 1986, Nb and Pb in oceanic basalts: New constraints on mantle evolution: Earth and Planetary Science Letters, v. 79, p. 33–45, https://doi.org/10.1016/0012-821X(86)90038-5.

Hoskin, P.W., and Schaltegger, U., 2003, The composition of zircon and igneous and metamorphic petrogenesis: Reviews in Mineralogy and Geochemistry, v. 53, p. 27–62, https://doi.org/10.2113/0530027.

Hou, Z.Q., Gao, Y.F., Qu, X.M., Rui, Z.Y., and Mo, X.X., 2004, Origin of adakitic intrusives generated during mid-Miocene east–west extension in southern Tibet: Earth and Planetary Science Letters, v. 220, p. 139–155, https://doi.org/10.1016/S0012-821X(04)00007-X.

Jackson, S.E., Pearson, N.J., Griffin, W.L., and Belousova, E.A., 2004, The application of laser ablation–inductively coupled plasma–mass spectrometry to in situ U–Pb zircon geochronology: Chemical Geology, v. 211, p. 47–69, https://doi.org/10.1016/j.chemgeo.2004.06.017.

Ji, W.Q., Wu, F.Y., Chung, S.L., Li, J.X., and Liu, C.Z., 2009, Zircon U–Pb geochronology and Hf isotopic constraints on petrogenesis of the Gangdese batholith, southern Tibet: Chemical Geology, v. 262, p. 229–245, https://doi.org/10.1016/j.chemgeo.2009.01.020.

Ji, W.Q., Wu, F.Y., Chung, S.L., and Liu, C.Z., 2014, The Gangdese magmatic constraints on a latest Cretaceous lithospheric delamination of the Lhasa terrane, southern Tibet: Lithos, v. 210–211, p. 168–180, https://doi.org/10.1016/j.lithos.2014.10.001.

Jiang, Z.Q., Wang, Q., Li, Z.X., Wyman, D.A., Tang, G.J., Jia, X.H., and Yang, Y.H., 2012, Late Cretaceous (ca. 90 Ma) adakitic intrusive rocks in the Kelu area, Gangdese belt (southern Tibet): Slab melting and implications for Cu–Au mineralization: Journal of Asian Earth Sciences, v. 53, p. 67–81, https://doi.org/10.1016/j.jseaes.2012.02.010.

Kapp, P., Yin, A., Harrison, T.M., and Ding, L., 2005, Cretaceous–Tertiary shortening, basin development, and volcanism in central Tibet: Geological Society of America Bulletin, v. 117, p. 865–878, https://doi.org/10.1130/B25595.1.

Karsli, O., Dokuz, A., and Kandemir, R., 2017, Zircon Lu–Hf isotope systematics and U–Pb geochronology, whole-rock Sr–Nd isotopes and geochemistry of the early Jurassic Gokcedere Pluton, Sakarya Zone-NE Turkey: A magmatic response to roll-back of the Paleo-Tethyan oceanic lithosphere: Contributions to Mineralogy and Petrology, v. 172, p. 1–27, https://doi.org/10.1007/s00410-017-1346-0.

Kelemen, P.B., Hanghøj, K., and Greene, A.R., 2003, One view of the geochemistry of subduction-related magmatic arcs, with an emphasis on primitive andesite and lower crust: Treatise on Geochemistry, v. 3, p. 659.

Kinzler, R.J., 1997, Melting of mantle peridotite at pressures approaching the spinel to garnet transition: Application to mid-ocean ridge basalt petrogenesis: Journal of Geophysical Research: Solid Earth, v. 102, p. 853–874, https://doi.org/10.1029/96JB00988.

Kiss, B., Harangi, S., Ntaflos, T., Mason, P.R.D., and Pál-Molnár, E., 2014, Amphibole perspective to unravel pre-eruptive processes and conditions in volcanic plumbing systems beneath intermediate arc volcanoes: A case study from Ciomadul volcano (SE Carpathians): Contributions to Mineralogy and Petrology, v. 167, https://doi.org/10.1007/s00410-014-0986-6.

Klaver, M., Matveev, S., Berndt, J., Lissenberg, C.J., and Vroon, P.Z., 2017, A mineral and cumulate perspective to magma differentiation at Nisyros volcano, Aegean arc: Contributions to Mineralogy and Petrology, v. 172, p. 1–23, https://doi.org/10.1007/s00410-017-1414-5.

Klein, B.Z., Jagoutz, O., and Ramezani, J., 2021, High-precision geochronology requires that ultrafast mantle-derived magmatic fluxes built the transcrustal Bear Valley Intrusive Suite, Sierra Nevada, California, USA: Geology, v. 49, p. 106–110, https://doi.org/10.1130/G47952.1.

Lackey, J.S., Cecil, M.R., Windham, C.J., Frazer, R.E., Bindeman, I.N., and Gehrels, G.E., 2012, The Fine Gold Intrusive Suite: The roles of basement terranes and magma source development in the Early Cretaceous Sierra Nevada batholith: Geosphere, v. 8, p. 292–313, https://doi.org/10.1130/GES00745.1.

Leake, B.E., Woolley, A.R., Arps, C.E.S., Birch, W.D., Gilbert, M.C., Grice, J.D., Hawthorne, F.C., Kato, A., Kisch, H.J., Krivovichev, V.G., Linthout, K., Laird, J., Mandarino, J.A., Maresch, W.V., Nickel, E.H., Rock, N.M.S., Schumacher, J.C., Smith, D.C., Stephenson, N.C.N., Ungaretti, L., Whittaker, E.J.W., and Guo, Y.Z., 1997, Nomenclature of Amphiboles: Report of the Subcommittee on Amphiboles of the International Mineralogical Association Commission on New Minerals and Mineral Names: Mineralogical Magazine, v. 61, p. 295–310, https://doi.org/10.1180/minmag.1997.061.405.13.

Lee, C.T.A., and Bachmann, O., 2014, How important is the role of crystal fractionation in making intermediate magmas? Insights from Zr and P systematics: Earth and Planetary Science Letters, v. 393, p. 266–274, https://doi.org/10.1016/j.epsl.2014.02.044.

Leier, A.L., DeCelles, P.G., Kapp, P., and Ding, L., 2007a, The Takena Formation of the Lhasa terrane, southern Tibet: The record of a Late Cretaceous retroarc foreland basin: Geological Society of America Bulletin, v. 119, p. 31–48, https://doi.org/10.1130/B25974.1.

Leier, A.L., Kapp, P., Gehrels, G.E., and DeCelles, P.G., 2007b, Detrital zircon geochronology of Carboniferous–Cretaceous strata in the Lhasa terrane, Southern Tibet: Basin Research, v. 19, p. 361–378, https://doi.org/10.1111/j.1365-2117.2007.00330.x.

Ludwig, K.R., 2003, User's Manual for Isoplot 3.00, a Geochronological Toolkit for Microsoft Excel: Berkeley Geochronology Center Special Publication 4, 70 p.

Ma, L., Wang, Q., Li, Z.X., Wyman, D.A., Jiang, Z.Q., Yang, J.H., Gou, G.N., and Guo, H.F., 2013a, Early Late Cretaceous (ca. 93 Ma) norites and hornblendites in the Milin area, eastern Gangdese: Lithosphere–asthenosphere interaction during slab roll-back and an insight into early Late Cretaceous (ca. 100–80 Ma) magmatic "flare-up" in southern Lhasa (Tibet): Lithos, v. 172–173, p. 17–30, https://doi.org/10.1016/j.lithos.2013.03.007.

Ma, L., Wang, Q., Wyman, D.A., Jiang, Z.Q., Wu, F.Y., Li, X.H., Yang, J.H., and Guo, H.F., 2015, Late Cretaceous back-arc extension and arc system evolution in the Gangdese area, southern Tibet: Geochronological, petrological, and Sr-Nd-Hf-O isotopic evidence from Dagze diabases: Journal of Geophysical Research: Solid Earth, v. 120, p. 6159–6181, https://doi.org/10.1002/2015JB011966.

Ma, L., Wang, Q., Wyman, D.A., Li, Z.X., Jiang, Z.Q., Yang, J.H., Gou, G.N., and Guo, H.F., 2013b, Late Cretaceous (100–89 Ma) magnesian charnockites with adakitic affinities in the Milin area, eastern Gangdese: Partial melting of subducted oceanic crust and implications for crustal growth in southern Tibet: Lithos, v. 175–176, p. 315–332, https://doi.org/10.1016/j.lithos.2013.04.006.

Ma, X., Xu, Z., and Meert, J.G., 2017, Syn-convergence extension in the southern Lhasa terrane: Evidence from Late Cretaceous adakitic granodiorite and coeval gabbroic-dioritic dikes: Journal of Geodynamics, v. 110, p. 12–30, https://doi.org/10.1016/j.jog.2017.07.004.

Martin, H., Smithies, R.H., Rapp, R., Moyen, J.F., and Champion, D., 2005, An overview of adakite, tonalite–trondhjemite–granodiorite (TTG), and sanukitoid: Relationships and some implications for crustal evolution: Lithos, v. 79, p. 1–24, https://doi.org/10.1016/j.lithos.2004.04.048.

McDonough, W.F., and Sun, S.S., 1995, The composition of the Earth: Chemical Geology, v. 120, p. 223–253, https://doi.org/10.1016/0009-2541(94)00140-4.

Middlemost, E.A., 1994, Naming materials in the magma/igneous rock system: Earth-Science Reviews, v. 37, p. 215–224, https://doi.org/10.1016/0012-8252(94)90029-9.

Mo, X., Hou, Z., Niu, Y., Dong, G., Qu, X., Zhao, Z., and Yang, Z., 2007, Mantle contributions to crustal thickening during continental collision: Evidence from Cenozoic igneous rocks in southern Tibet: Lithos, v. 96, p. 225–242, https://doi.org/10.1016/j.lithos.2006.10.005.

Mo, X., Niu, Y., Dong, G., Zhao, Z., Hou, Z., Zhou, S., and Ke, S., 2008, Contribution of syncollisional felsic magmatism to continental crust growth: A case study of the Paleogene Linzizong volcanic succession in southern Tibet: Chemical Geology, v. 250, p. 49–67, https://doi.org/10.1016/j.chemgeo.2008.02.003.

Moyen, J.F., Janoušek, V., Laurent, O., Bachmann, O., Jacob, J.B., Farina, F., and Villaros, A., 2021, Crustal melting vs. fractionation of basaltic magmas: Part 1, granites and paradigms: Lithos, v. 402–403, https://doi.org/10.1016/j.lithos.2021.106291.

Palme, H., and O'Neill, H.S.C., 2004, Cosmochemical estimates of mantle composition, *in* Holland H.D., and Turekian K.K., eds., Treatise on Geochemistry 2: Amsterdam, Elsevier, p. 1–38.

Patiño Douce, A.E., and Harris, N., 1998, Experimental constraints on Himalayan anatexis: Journal of Petrology, v. 39, p. 689–710, https://doi.org/10.1093/petroj/39.4.689.

Pearce, J.A., 2014, Immobile element fingerprinting of ophiolites: Elements (Midland), v. 10, p. 101–108, https://doi.org/10.2113/gselements.10.2.101.

Peccerillo, A., and Taylor, S.R., 1976, Geochemistry of Eocene calc-alkaline volcanic rocks from the Kastamonu area, northern Turkey: Contributions to Mineralogy and Petrology, v. 58, p. 63–81, https://doi.org/10.1007/BF00384745.

Petford, N., and Gallagher, K., 2001, Partial melting of mafic (amphibolitic) lower crust by periodic influx of basaltic magma: Earth and Planetary Science Letters, v. 193, p. 483–499, https://doi.org/10.1016/S0012-821X(01)00481-2.

Pistone, M., Blundy, J., and Brooker, R.A., 2017, Water transfer during magma mixing events: Insights into crystal mush rejuvenation and melt extraction processes: The American Mineralogist, v. 102, p. 766–776, https://doi.org/10.2138/am-2017-5793.

Plank, T., and Langmuir, C.H., 1988, An evaluation of the global variations in the major element chemistry of arc basalts: Earth and Planetary Science Letters, v. 90, no. 4, p. 349–370, https://doi.org/10.1016/0012-821X(88)90135-5.

Profeta, L., Ducea, M.N., Chapman, J.B., Paterson, S.R., Gonzales, S.M.H., Kirsch, M., Petrescu, L., and DeCelles, P.G., 2015, Quantifying crustal thickness over time in magmatic arcs: Scientific Reports, v. 5, https://doi.org/10.1038/srep17786.

Pu, W., Gao, J., Zhao, K., Ling, H., and Jiang, S., 2005, Separation method of Rb–Sr, Sm–Nd using DCTA and HIBA: Acta Geoscientica Sinica, v. 41, p. 445–450.

Ratajeski, K., Glazner, A.F., and Miller, B.V., 2001, Geology and geochemistry of mafic to felsic plutonic rocks in the Cretaceous intrusive suite of Yosemite Valley, California: Geological Society of America Bulletin, v. 113, p. 1486–1502, https://doi.org/10.1130/0016-7606(2001)113<1486:GAGOMT>2.0.CO;2.

Richards, J.P., and Kerrich, R., 2007, Special paper: Adakite-like rocks: Their diverse origins and questionable role in metallogenesis: Economic Geology, v. 102, p. 537–576, https://doi.org/10.2113/gsecongeo.102.4.537.

Ridolfi, F., Renzulli, A., and Puerini, M., 2010, Stability and chemical equilibrium of amphibole in calc-alkaline magmas: an overview, new thermobarometric formulations and application to subduction-related volcanoes: Contributions to Mineralogy and Petrology, v. 160, p. 45–66, https://doi.org/10.1007/s00410-009-0465-7.

Rong, W., Zhang, S.B., and Zheng, Y.F., 2017, Back-reaction of peritectic garnet as an explanation for the origin of mafic enclaves in S-type granite from the Jiuling batholith in South China: Journal of Petrology, v. 58, p. 569–598, https://doi.org/10.1093/petrology/egx029.

Rudnick, R.L., 1995, Making continental crust: Nature, v. 378, p. 571–578, https://doi.org/10.1038/378571a0.

Rudnick, R.L., and Gao, S., 2003, Composition of the continental crust, *in* Holland, H.D., and Turekian, eds., Treatise on Geochemistry: Amsterdam, Netherlands, Elsevier, v. 3, p. 1–64, https://doi.org/10.1016/B0-08-043751-6/03016-4.

Shand, S.J., 1943, Eruptive Rocks: Their Genesis, Composition, and Classification, and Their Relation to Ore-Deposits with a Chapter on Meteorites: New York, USA, John Wiley & Sons, 444 p.

Shaw, D.M., 1970, Trace element fractionation during anatexis: Geochimica et Cosmochimica Acta, v. 34, p. 237–243, https://doi.org/10.1016/0016-7037(70)90009-8.

Shaw, D.M., 2000, Continuous (dynamic) melting theory revisited: Canadian Mineralogist, v. 38, p. 1041–1063, https://doi.org/10.2113/gscanmin.38.5.1041.

Sisson, T.W., and Bronto, S., 1998, Evidence for pressure-release melting beneath magmatic arcs from basalt at Galunggung, Indonesia: Nature, v. 391, p. 883–886, https://doi.org/10.1038/36087.

Słaby, E., and Martin, H., 2008, Mafic and felsic magma interaction in granites: The Hercynian Karkonosze Pluton (Sudetes, Bohemian Massif): Journal of Petrology, v. 49, p. 353–391, https://doi.org/10.1093/petrology/egm085.

Smith, E.I., Sanchez, A., Walker, J.D., and Wang, K., 1999, Geochemistry of mafic magmas in the Hurricane Volcanic field, Utah: Implications for small-and large-scale chemical variability of the lithospheric mantle: The Journal of Geology, v. 107, p. 433–448, https://doi.org/10.1086/314355.

Söderlund, U., Patchett, P.J., Vervoort, J.D., and Isachsen, C.E., 2004, The ^{176}Lu decay constant determined by Lu–Hf and U–Pb isotope systematics of Precambrian mafic intrusions: Earth and Planetary Science Letters, v. 219, p. 311–324, https://doi.org/10.1016/S0012-821X(04)00012-3.

Sparks, R.S.J., and Marshall, L.A., 1986, Thermal and mechanical constraints on mixing between mafic and silicic magmas: Journal of Volcanology and Geothermal Research, v. 29, p. 99–124, https://doi.org/10.1016/0377-0273(86)90041-7.

Stern, C.R., and Kilian, R., 1996, Role of the subducted slab, mantle wedge and continental crust in the generation of adakites from the Andean Austral Volcanic Zone: Contributions to Mineralogy and Petrology, v. 123, p. 263–281, https://doi.org/10.1007/s004100050155.

Sun, S.S., and McDonough, W.F., 1989, Chemical and isotopic systematics of oceanic basalts: Implications for mantle composition and processes, *in* Saunders, A.D., and Norry, M.J., eds., Magmatism in the Ocean Basins: Geological Society, London, Special Publication 42, p. 313–345, https://doi.org/10.1144/GSL.SP.1989.042.01.19.

Sundell, K.E., Laskowski, A.K., Kapp, P.A., Ducea, M., and Chapman, J.B., 2021, Jurassic to Neogene quantitative crustal thickness estimates in Southern Tibet: GSA Today, v. 31, p. 4–10, https://doi.org/10.1130/GSATG461A.1.

Szymanowski, D., Wotzlaw, J.-F., Ellis, B.S., Bachmann, O., Guillong, M., and von Quadt, A., 2017, Protracted near-solidus storage and pre-eruptive rejuvenation of large magma reservoirs: Nature Geoscience, v. 10, p. 777–782, https://doi.org/10.1038/ngeo3020.

Tamura, Y., Tatsumi, Y., Zhao, D., Kido, Y., and Shukuno, H., 2002, Hot fingers in the mantle wedge: New insights into magma genesis in subduction zones: Earth and Planetary Science Letters, v. 197, p. 105–116, https://doi.org/10.1016/S0012-821X(02)00465-X.

Tang, M., Ji, W.Q., Chu, X., Wu, A., and Chen, C., 2021, Reconstructing crustal thickness evolution from europium anomalies in detrital zircons: Geology, v. 49, p. 76–80, https://doi.org/10.1130/G47745.1.

Tavazzani, L., Peres, S., Sinigoi, S., Demarchi, G., Economos, R.C., and Quick, J.E., 2020, Timescales and mechanisms of crystal-mush rejuvenation and melt extraction recorded in Permian plutonic and volcanic rocks of the Sesia Magmatic System (southern Alps, Italy): Journal of Petrology, v. 61, https://doi.org/10.1093/petrology/egaa049.

Turnbull, R., Weaver, S., Tulloch, A., Cole, J., Handler, M., and Ireland, T., 2010, Field and geochemical constraints on mafic–felsic interactions, and processes in high-level arc magma chambers: An example from the Halfmoon Pluton, New Zealand: Journal of Petrology, v. 51, p. 1477–1505, https://doi.org/10.1093/petrology/egq026.

Turner, S., Hawkesworth, C., Liu, J., Rogers, N., Kelley, S., and Van Calsteren, P., 1993, Timing of Tibetan uplift constrained by analysis of volcanic rocks: Nature, v. 364, p. 50–54, https://doi.org/10.1038/364050a0.

Turner, S.J., and Langmuir, C.H., 2015, The global chemical systematics of arc front stratovolcanoes: Evaluating the role of crustal processes: Earth and Planetary Science Letters, v. 422, p. 182–193, https://doi.org/10.1016/j.epsl.2015.03.056.

Turner, S.J., and Langmuir, C.H., 2022, An evaluation of five models of arc volcanism: Journal of Petrology, v. 63, p. 1–25, https://doi.org/10.1093/petrology/egac010.

Vernon, R.H., 1984, Microgranitoid enclaves in granites—globules of hybrid magma quenched in a plutonic environment: Nature, v. 309, p. 438–439, https://doi.org/10.1038/309438a0.

Walter, M.J., 1998, Melting of garnet peridotite and the origin of komatiite and depleted lithosphere: Journal of Petrology, v. 39, p. 29–60, https://doi.org/10.1093/petroj/39.1.29.

Wang, J.G., Hu, X., Garzanti, E., BouDagher-Fadel, M.K., Liu, Z.C., Li, J., and Wu, F.Y., 2020, From extension to tectonic inversion: Mid-Cretaceous onset of Andean-type orogeny in the Lhasa block and early topographic growth of Tibet: Geological Society of America Bulletin, v. 132, p. 2432–2454, https://doi.org/10.1130/B35314.1.

Wang, Q., Xu, J.F., Jian, P., Bao, Z.W., Zhao, Z.H., Li, C.F., Xiong, X.L., and Ma, J.L., 2006, Petrogenesis of adakitic porphyries in an extensional tectonic setting, Dexing, South China: Implications for the genesis of porphyry copper mineralization: Journal of Petrology, v. 47, p. 119–144, https://doi.org/10.1093/petrology/egi070.

Wang, R.Q., Qiu, J.S., Wen, D.J., and Xu, H., 2021, The role of hydrous mantle-derived magmas in the generation of Late Cretaceous granitoids in the Gangdese batholith: Insights from the Shanba and Zongga plutons in the southern Lhasa subterrane, Tibet: Mineralogy and Petrology, v. 115, p. 113–136, https://doi.org/10.1007/s00710-020-00728-6.

Weinberg, R.F., Vernon, R.H., and Schmeling, H., 2021, Processes in mushes and their role in the differentiation of granitic rocks: Earth-Science Reviews, v. 220, https://doi.org/10.1016/j.earscirev.2021.103665.

Wen, D.R., Chung, S.L., Song, B., Iizuka, Y., Yang, H.J., Ji, J., Liu, D.Y., and Gallet, S., 2008, Late Cretaceous Gangdese intrusions of adakitic geochemical characteristics, SE Tibet: Petrogenesis and tectonic implications: Lithos, v. 105, p. 1–11, https://doi.org/10.1016/j.lithos.2008.02.005.

Wiebe, R.A., Smith, D., Sturm, M., King, E.M., and Seckler, M.S., 1997, Enclaves in the Cadillac mountain granite (Coastal Maine): Samples of hybrid magma from the base of the chamber: Journal of Petrology, v. 38, p. 393–423, https://doi.org/10.1093/petroj/38.3.393.

Woodhead, J.D., and Hergt, J.M., 2005, A preliminary appraisal of seven natural zircon reference materials for in situ Hf isotope determination: Geostandards and Geoanalytical Research, v. 29, p. 183–195, https://doi.org/10.1111/j.1751-908X.2005.tb00891.x.

Workman, R.K., and Hart, S.R., 2005, Major and trace element composition of the depleted MORB mantle (DMM): Earth and Planetary Science Letters, v. 231, p. 53–72, https://doi.org/10.1016/j.epsl.2004.12.005.

Wu, F.Y., Yang, Y.H., Xie, L.W., Yang, J.H., and Xu, P., 2006, Hf isotopic compositions of the standard zircons and baddeleyites used in U–Pb geochronology: Chemical Geology, v. 234, p. 105–126, https://doi.org/10.1016/j.chemgeo.2006.05.003.

Xu, J.F., and Castillo, P.R., 2004, Geochemical and Nd–Pb isotopic characteristics of the Tethyan asthenosphere: Implications for the origin of the Indian Ocean mantle domain: Tectonophysics, v. 393, p. 9–27, https://doi.org/10.1016/j.tecto.2004.07.028.

Xu, W., Zhu, D.C., Wang, Q., Weinberg, R.F., Wang, R., Li, S.M., Zhang, L.L., and Zhao, Z.D., 2019, Constructing the Early Mesozoic Gangdese crust in southern Tibet by hornblende-dominated magmatic differentiation: Journal of Petrology, v. 60, p. 515–552, https://doi.org/10.1093/petrology/egz005.

Xu, W.C., Zhang, H.F., Luo, B.J., Guo, L., and Yang, H., 2015, Adakite-like geochemical signature produced by amphibole-dominated fractionation of arc magmas: An example from the Late Cretaceous magmatism in Gangdese belt, south Tibet: Lithos, v. 232, p. 197–210, https://doi.org/10.1016/j.lithos.2015.07.001.

Yin, A., and Harrison, T.M., 2000, Geologic evolution of the Himalayan-Tibetan orogen: Annual Review of Earth and Planetary Sciences, v. 28, p. 211–280, https://doi.org/10.1146/annurev.earth.28.1.211.

Yin, C., Ou, J., Long, X., Huang, F., Zhang, J., Li, S., Wang, L.J., Xia, X.P., and He, X., 2020, Late Cretaceous Neo-Tethyan slab roll-back: Evidence from zircon U–Pb–O and whole-rock geochemical and Sr–Nd–Fe isotopic data of adakitic plutons in the Himalaya-Tibetan Plateau: Geological Society of America Bulletin, v. 132, p. 409–426, https://doi.org/10.1130/B35242.1.

Yogodzinski, G.M., Kay, R.W., Volynets, O.N., Koloskov, A.V., and Kay, S.M., 1995, Magnesian andesite in the western Aleutian Komandorsky region: Implications for slab melting and processes in the mantle wedge: Geological Society of America Bulletin, v. 107, p. 505–519, https://doi.org/10.1130/0016-7606(1995)107<0505:MAITWA>2.3.CO;2.

Zhang, S.Q., Mahoney, J.J., Mo, X.X., Ghazi, A.M., Milani, L., Crawford, A.J., Guo, T.Y., and Zhao, Z.D., 2005, Evidence for a widespread Tethyan upper mantle with Indian Ocean-type isotopic characteristics: Journal of Petrology, v. 46, p. 829–858, https://doi.org/10.1093/petrology/egi002.

Zhang, Z., Zhao, G., Santosh, M., Wang, J., Dong, X., and Shen, K., 2010, Late Cretaceous charnockite with adakitic affinities from the Gangdese batholith, southeastern Tibet: Evidence for Neo-Tethyan mid-ocean ridge subduction?: Gondwana Research, v. 17, p. 615–631, https://doi.org/10.1016/j.gr.2009.10.007.

Zhang, Z.M., Ding, H.X., Dong, X., Tian, Z.L., Palin, R.M., Santosh, M., Chen, Y.F., Jiang, Y.Y., Qing, S.K., Kang, D.Y., and Li, W.T., 2022, The Mesozoic magmatic, metamorphic, and tectonic evolution of the eastern Gangdese magmatic arc, southern Tibet: Geological Society of America Bulletin, v. 134, p. 1721–1740, https://doi.org/10.1130/B36134.1.

Zhu, D.C., Mo, X.X., Niu, Y., Zhao, Z.D., Wang, L.Q., Liu, Y.S., and Wu, F.Y., 2009, Geochemical investigation of Early Cretaceous igneous rocks along an east–west traverse throughout the central Lhasa terrane, Tibet: Chemical Geology, v. 268, p. 298–312, https://doi.org/10.1016/j.chemgeo.2009.09.008.

Zhu, D.C., Zhao, Z.D., Niu, Y., Mo, X.X., Chung, S.L., Hou, Z.Q., Wang, L.Q., and Wu, F.Y., 2011, The Lhasa terrane: Record of a microcontinent and its histories of drift and growth: Earth and Planetary Science Letters, v. 301, no. 1–2, p. 241–255, https://doi.org/10.1016/j.epsl.2010.11.005.

Zhu, D.C., Zhao, Z.D., Niu, Y., Dilek, Y., Hou, Z.Q., and Mo, X.X., 2013, The origin and pre-Cenozoic evolution of the Tibetan Plateau: Gondwana Research, v. 23, no. 4, p. 1429–1454, https://doi.org/10.1016/j.gr.2012.02.002.

Zhu, D.C., Wang, Q., Cawood, P.A., Zhao, Z.D., and Mo, X.X., 2017, Raising the Gangdese mountains in southern Tibet: Journal of Geophysical Research: Solid Earth, v. 122, no. 1, p. 214–223, https://doi.org/10.1002/2016JB013508.

Zong, K.Q., Klemd, R., Yuan, Y., He, Z.Y., Guo, J.L., Shi, X.L., Liu, Y.S., Hu, Z.C., and Zhang, Z.M., 2017, The assembly of Rodinia: The correlation of early Neoproterozoic (ca. 900 Ma) high-grade metamorphism and continental arc formation in the southern Beishan Orogen, southern Central Asian Orogenic Belt (CAOB): Precambrian Research, v. 290, p. 32–48, https://doi.org/10.1016/j.precamres.2016.12.010.

Science Editor: Wenjiao Xiao
Associate Editor: Shan Li

Manuscript Received 28 March 2022
Revised Manuscript Received 14 September 2022
Manuscript Accepted 17 October 2022

Printed in the USA